Czech Technical University in Prague
Faculty of Electrical Engineering

BACHELOR PROJECT

Modeling and control of piezoelectric microactuators

Jiří Figura

Praha, 2013 **Supervisor: Ing. Zdeněk Hurák, PhD.**

Czech Technical University in Prague
Faculty of Electrical Engineering

Department of Control Engineering

BACHELOR PROJECT ASSIGNMENT

Student: **Jiří Figura**

Study programme: Cybernetics and Robotics
Specialisation: Systems and Control

Title of Bachelor Project: **Modeling and control of piezoelectric microactuators**

Guidelines:

1. Build mathematical models for a few provided piezoelectric micromanipulators (linear stack, ultrasonic, ...)
2. Verify the mathematical models using laboratory experiments.
3. Analyze a few selected control design problems, give a survey of existing approaches, demonstrate the functionality of the approaches using simulations and laboratory experiments.

Bibliography/Sources:

[1] A. Bergander, Control, wear testing and integration of stick-slip micropositioning, Ph.D. thesis, EPFL, 2003.
[2] J.-M. Breguet and R. Clavel, Stick and slip actuators: design, control, performances and applications, in Proceedings of IEEE International Symposium on Micromechatronics and Human Science, 1998, pp. 89-95.
[3] T. Ikeda, Fundamentals of Piezoelectricity. Oxford University Press, USA, 1990.
[4] S. O. R. Moheimani and A. J. Fleming, Piezoelectric Transducers for Vibration Control and Damping, 1st ed. Springer, 2006.
[5] IEEE standard on piezoelectricity - ANSI/IEEE Std 176-1987, ANSI/IEEE Std 176-1987, 1988.

Bachelor Project Supervisor: Ing. Zdeněk Hurák, Ph.D.

Valid until the winter semester 2013/2014

L.S.

prof. Ing. Michael Šebek, DrSc.
Head of Department

prof. Ing. Pavel Ripka, CSc.
Dean

Prague, January 22, 2013

Acknowledgments

I would like to thank my supervisor Zdeněk Hurák and Jiří Zemánek for their advice and assistance.

Declaration

I hereby declare that this project is my own work and that I have listed all the literature and publications used in accordance with *Metodický pokyn č. 1/2009 – O dodržování etických principů při přípravě vysokoškolských závěrečných prací.*

In Prague on May 24, 2013 .....

Abstract

This project deals with modeling and control of two types of piezoelectric actuators. In particular, two lumped-parameter models were developed for a provided commercially available stack actuator. Great emphasis is given to modeling of hysteresis – a major nonlinear phenomenon present in the stack actuator – by phenomenological models. Quality of the models is validated by comparison of model simulations and real actuator displacement measurements acquired by optical interferometer.

Results show that all introduced models describe the behavior of the stack actuator very well. Inverses of the models are subsequently used for design of feedforward hysteresis compensators. Simulations prove that hysteresis can be compensated perfectly by model inverses; measurements show that hysteresis in real stack actuator can be compensated with very good results.

The other piezoelectric actuator investigated in this project was commercially available linear plate ultrasonic actuator. Closed-loop operation of the actuator was not possible due to low interferometer real-time sampling rate, hence a few practical experiments with open-loop control were conducted. These indicated that the actuator is difficult to control in open-loop due to the highly nonlinear behavior.

Abstrakt

Tato práce se zabývá modelováním a řízením dvou typů piezoelektrických aktuátorů. Pro komerčně dostupný stack aktuátor byly vytvořeny dva modely se soustředěnými parametery. Velký důraz je kladen na modelování hystereze – významného nelineárního jevu přítomného ve stack aktuátorech – pomocí fenomenologických modelů. Kvalita použitých modelů je ověřena porovnáním jejich simulací s měřeními na reálném stack aktuátoru. K těmto měřením je použit optický interferometr.

Výsledky ukazují, že všechny představené modely velmi dobře popisují chování stack aktuátoru. Inverze hysterezních modelů jsou následně využity v řízení jako dopředné regulátory sloužící ke kompenzaci hystereze. Simulace dokazují, že hysterezi lze inverzními modely dokonale kompenzovat. Měření potvrzují, že hysterezi lze kompenzovat s velmi dobrými výsledky i u reálného aktuátoru.

Druhým zkoumaným piezoelektrickým aktuátorem byl komerčně dostupný lineární "plate" ultrazvukový aktuátor. Protože řízení v uzavřené smyčce nebylo možné vzhledem k nízké vzorkovací frekvenci interferometru v reálném čase, byly provedeny experimenty s řízením v otevřené smyčce, které ukázaly, že je tímto způsobem aktuátor obtížně řiditelný vzhledem k jeho vysoce nelineárnímu chování.

Contents

Chapter 1

Introduction

During the past few decades, piezoelectric devices have become very important part of today's modern engineering. Their importance is growing with increasing demands for miniaturization and higher precision positioning. It is one of the goals of the project to get familiar with this broad subject connected to many other scientific and engineering disciplines. Since system modeling and control engineering are the main subjects of my study, exploring piezoelectric devices with tools provided by these disciplines was a great idea that led to selection of the topic for my bachelor project.

This project deals with modeling and control of two types of piezoelectric actuators. In particular, a stack actuator and ultrasonic plate actuator. Two lumped-parameter models were developed for a provided commercially available stack actuator. Since hysteresis is a major nonlinear phenomenon present in the stack actuator, a great emphasis is given to its modeling by phenomenological models. Quality of the models is validated by comparison of model simulations and real actuator displacement measurements acquired by optical interferometer, a high resolution displacement measuring device.

Results show that all introduced models describe the behavior of the stack actuator very well. Inverses of the models are subsequently used for design of feedforward hysteresis compensators. Simulations prove that hysteresis can be compensated perfectly by model inverses; measurements show that hysteresis in real stack actuator can be compensated with very good results.

The other piezoelectric actuator investigated in this project was commercially available linear plate ultrasonic actuator. Closed-loop operation of the actuator turned out not to be possible due to low interferometer real-time sampling rate, hence a few practical experiments with open-loop control were conducted. These indicated that the actuator is difficult to control in open-loop due to the highly nonlinear behavior.

For reader's comfort piezoelectric effect is introduced in Chapter 2. Chapter 3 presents piezoelectric actuators and focuses on two types in detail. Chapter 4 makes the reader acquainted with an optical interferometer. Its working principle is explained and commercially available device from SIOS Meßtechnik is examined. In Chapter 5 two lumped-parameter models and three hysteresis models of the stack actuator are presented. In the following chapter these models are simulated and compared to a real stack actuator. Chapter 7 describes hysteresis compensation of stack actuator by inverses of the models developed in previous chapters. Chapter 8 suggests a simple ultrasonic actuator model and summarizes experiments performed on commercially available ultrasonic actuator.

Chapter 2

Principles of piezoelectricity

This chapter serves as an introduction of piezoelectricity and summarizes general knowledge about the topic. The chapter starts with a brief introduction of piezoelectric effect and its manifestation in piezoceramics. Before discussing electrical and mechanical properties of piezoceramics a mathematical description of the piezoelectric effect is given. The chapter concludes with a reference to nonlinear phenomena that appear in the piezoceramic materials. One of these phenomena, hysteresis, is discussed in more detail in later chapters.

2.1 Piezoelectric effect

Piezoelectric effect is a property of certain solid materials with crystalline structure. These materials respond to mechanical deformation by creating electric charge on their surface. They also exhibit so called converse piezoelectric effect – an application of electric field results in mechanical strain. These materials are naturally occurring crystals (e.g. quartz, topaz, sucrose) or synthetic ones, certain biological materials (e.g. bone, DNA, wood) and most importantly synthetic ceramics, materials developed to exhibit sufficiently strong piezoelectric effect for practical use.

2.2 Piezoelectric effect in ceramics

There are many synthetic ceramics developed to exhibit piezoelectric effect. The first ceramic discovered was Barium titanate ($BaTiO_3$). There are for example Lithium niobate, Lithium tantalate, Sodium tungstate and many more. Currently the most frequently used are variations of PZT – lead zirconate titanate.

2.2.1 PZT manufacture

Lead zirconate titanate (PZT) manufacture is started by mixing metal powders. The mixture is heated and an organic binder is added. The resulting substance is formed into required shapes, such as rings, disks, rods, thin plates etc. and then heated until a crystalline structure is formed. Fig. 2.1 shows a PZT lattice. When the material is deformed, there is an asymmetry in the crystal lattice, therefore the material has nonzero polarization. When subject to temperature lower than so called Curie temperature the PZT as a ferroelectric material consists of spontaneously polarized electric dipole domains.

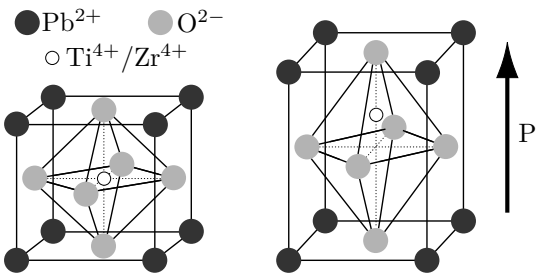

Figure 2.1: A PZT lattice [1].

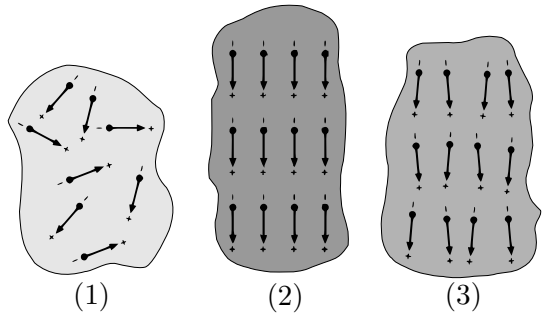

Figure 2.2: Electric dipole domains in PZT [2].

We can think of the domain as a group of lattices polarized in the same direction. Since these domains are random, there is no total polarization in the material (Fig. 2.2(1)). By applying an electric field at temperature a little lower than Curie temperature, the orientation of polarization in every domain gets aligned with orientation of the electric field and the material is also elongated in that direction (Fig. 2.2(2)). After the field is removed the orientation of the domains remains nearly aligned (Fig. 2.2(3)) and the material is then permanently polarized. This so called poling process gives piezoceramics the required properties for practical use.

2.2.2 Soft and Hard PZT

The lead, zirconium an titanium are not the only elements the PZT is made from. By adding Na^{+1} or Fe^{+3} we can create a PZT with decreased domain wall mobility, i.e. with weaker piezoelectric effect, but with lower material losses. It is called *hard PZT*. Hard PZT is often used in resonators and high-power ultrasonic applications. *Soft PZT* is doped with La^{+3} or Nb^{+5}. It exhibits stronger piezoelectric effect and it is used in sensors and actuators.

2.2.3 Lead-free ceramics

There are growing concerns about using certain hazardous substances such as lead. There are millions of PZT devices sold every year. Although their usage is risk-free, their disposal is an issue. *The Directive on the restriction of the use of certain hazardous substances in electrical and electronic equipment* (RoHS) adopted in 2006 by the European Union fueled the development of lead-free piezoelectric ceramics. The PZT ceramic was given temporary exception from the restrictions due to the lack of lead-free ceramics with comparable properties. There are several candidates for replacing PZT such as sodium potassium niobate [3], bismuth ferrite or bismuth sodium titanate.

2.3 Mathematical description

Both piezoelectric and converse piezoelectric effect are most often mathematically described by a set of equations published in IEEE Standard on Piezoelectricity [4]. There are four forms to describe piezoelectricity according to the standard. Eq. 2.1 show the strain-charge form, which is most common.

$$\begin{aligned} S_p &= s^{\mathrm{E}}_{pq}\sigma_q + d^{\mathrm{T}}_{kp}E_k, \\ D_i &= d_{iq}\sigma_q + \varepsilon^{\sigma}_{ik}E_k, \end{aligned} \tag{2.1}$$

$$d_{iq} = d_{kp} = \left(\frac{\partial D_k}{\partial \sigma_p}\right)^{\mathrm{E}} = \left(\frac{\partial S_p}{\partial E_k}\right)^{\sigma}, \tag{2.2}$$

where i, $k = 1, 2, 3$; p, $q = 1, 2, ..., 6$. S_p is a strain tensor, s^{E}_{pq} is a compliance tensor, σ_q is a mechanical stress vector, d_{kp} is a matrix of piezoelectric charge constants, E_k is an electric field vector, D_i is an electric displacement vector and $\varepsilon^{\sigma}_{ik}$ is a matrix of permittivity. Superscript T denotes transposition, superscripts E and σ denote that the measurement was taken when subjected to constant electric field or under constant mechanical stress, respectively.

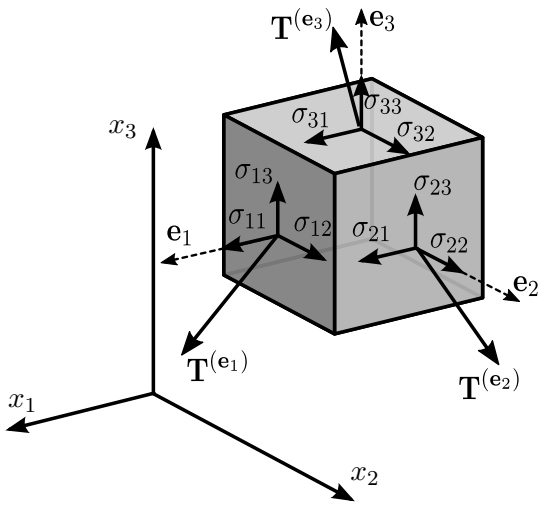

Figure 2.3: Stress tensor illustrated [1].

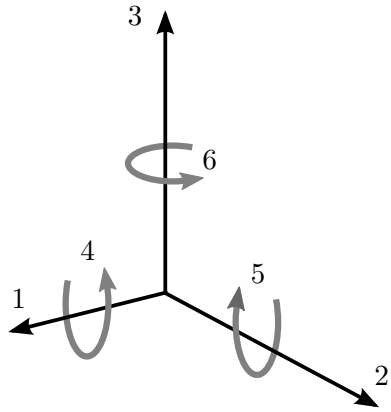

Figure 2.4: Stress tensor in Voigt notation.

Let us take a closer look at the notation used. Fig 2.3 illustrates the meaning of the stress tensor elements expressed in eq. 2.3. Since this tensor is symmetric, the number of unique elements in the tensor drops from 9 to 6. Therefore the stress tensor can be thought of as a stress along and around each coordinate axis as is shown in Fig. 2.4 and as is described by eq. 2.4.

$$\sigma_{ij} = \begin{bmatrix} \sigma_{11} & \sigma_{12} & \sigma_{13} \\ \sigma_{21} & \sigma_{22} & \sigma_{23} \\ \sigma_{31} & \sigma_{32} & \sigma_{33} \end{bmatrix}, \tag{2.3}$$

$$\begin{bmatrix} \sigma_1 & \sigma_2 & \sigma_3 & \sigma_4 & \sigma_5 & \sigma_6 \end{bmatrix} \equiv \begin{bmatrix} \sigma_{11} & \sigma_{22} & \sigma_{33} & \sigma_{23} & \sigma_{31} & \sigma_{12} \end{bmatrix}. \tag{2.4}$$

Let us assume the polarization along the third axis. Since the PZT is transversely isotropic material, there are many symmetries reducing the total number of unique elements. We can rewrite the eq. 2.1 to the form displayed in eq. 2.5.

$$\begin{bmatrix} S_1 \\ S_2 \\ S_3 \\ S_4 \\ S_5 \\ S_6 \end{bmatrix} = \begin{bmatrix} s_{11}^E & s_{12}^E & s_{13}^E & 0 & 0 & 0 \\ s_{12}^E & s_{11}^E & s_{13}^E & 0 & 0 & 0 \\ s_{13}^E & s_{13}^E & s_{33}^E & 0 & 0 & 0 \\ 0 & 0 & 0 & s_{44}^E & 0 & 0 \\ 0 & 0 & 0 & 0 & s_{44}^E & 0 \\ 0 & 0 & 0 & 0 & 0 & 2\left(s_{11}^E - s_{12}^E\right) \end{bmatrix} \begin{bmatrix} \sigma_1 \\ \sigma_2 \\ \sigma_3 \\ \sigma_4 \\ \sigma_5 \\ \sigma_6 \end{bmatrix} + \begin{bmatrix} 0 & 0 & d_{31} \\ 0 & 0 & d_{31} \\ 0 & 0 & d_{33} \\ 0 & d_{15} & 0 \\ d_{15} & 0 & 0 \\ 0 & 0 & 0 \end{bmatrix} \begin{bmatrix} E_1 \\ E_2 \\ E_3 \end{bmatrix}, \tag{2.5a}$$

$$\begin{bmatrix} D_1 \\ D_2 \\ D_3 \end{bmatrix} = \begin{bmatrix} 0 & 0 & 0 & 0 & d_{15} & 0 \\ 0 & 0 & 0 & d_{15} & 0 & 0 \\ d_{31} & d_{31} & d_{33} & 0 & 0 & 0 \end{bmatrix} \begin{bmatrix} \sigma_1 \\ \sigma_2 \\ \sigma_3 \\ \sigma_4 \\ \sigma_5 \\ \sigma_6 \end{bmatrix} + \begin{bmatrix} \varepsilon_{11} & 0 & 0 \\ 0 & \varepsilon_{11} & 0 \\ 0 & 0 & \varepsilon_{33} \end{bmatrix} \begin{bmatrix} E_1 \\ E_2 \\ E_3 \end{bmatrix}. \tag{2.5b}$$

Another form for describing the piezoelectric effect is the strain-voltage form:

$$\begin{aligned} S_p &= s_{pq}^{\mathrm{D}} \sigma_q + g_{kp}^{\mathrm{T}} D_k, \\ E_i &= -g_{iq} \sigma_q + \beta_{ik}^{\sigma} D_k, \end{aligned} \tag{2.6}$$

$$g_{iq} = g_{kp} = -\left(\frac{\partial E_k}{\partial T_p}\right)^{\mathrm{D}} = \left(\frac{\partial S_p}{\partial D_k}\right)^{\sigma}, \tag{2.7}$$

where $i, k = 1, 2, 3$; $p, q = 1, 2, ..., 6$. S_p is a strain tensor, s_{pq}^{D} is a compliance tensor, σ_q is a mechanical stress vector, g_{kp} is a matrix of piezoelectric voltage constants, E_i is an electric field vector, D_k is an electric displacement vector and β_{ik}^{σ} is an inverse of permittivity matrix. Superscript T denotes transposition, superscripts D and σ denote that the measurement was taken when subjected to constant electric displacement or under constant mechanical stress, respectively.

2.4 Piezoceramics properties and parameters

2.4.1 Documentation parameters

There are several piezoceramics parameters that appear in the documentation given by the manufacturers. Let us have a look at some of them.

Charge and voltage constants

As eq. 2.5 show, there are only three charge constants d_{31}, d_{33}, d_{15} that characterize the piezoceramics. To understand the notation, take d_{31}. It gives strain in direction 1 per unit electric field applied in direction 3 or it can be viewed as induced electric charge in direction 3 per unit stress applied in direction 1. Note that d_{31} constant is negative, in absolute values it is usually lower than d_{33} and d_{15}. The voltage constants are analogical, g_{31} denotes induced electric field in direction 3 per unit stress in direction 1.

Coupling factor

Coupling factor is a measure of efficiency of energy transfer between electrical and mechanical domains and vice versa. The coupling factor is a matrix denoted k_{ij}, where i, $j = 1, 2, ..., 6$. It is consistent with the notation introduced above. It is defined

$$k^2 = \frac{\text{energy converted}}{\text{energy input}}. \tag{2.8}$$

The eq. 2.8 can be also written in terms of piezoelectric constants. In the manufacturer's documentation there are usually four coupling factors specified. A planar coupling factor k_p for electric field in direction 3 and radial vibrations of a thin disc, k_{15}, k_{31} and k_{33}. First index denotes direction of electric field, the second one denotes direction of mechanical deformation. Usually k_{33} is the most efficient coupling factor, while k_{31} the lowest.

Frequency constants

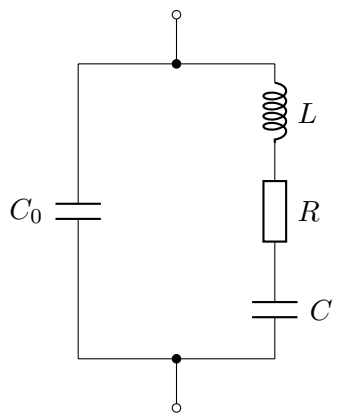

Figure 2.5: Equivalent circuit model for piezoceramics.

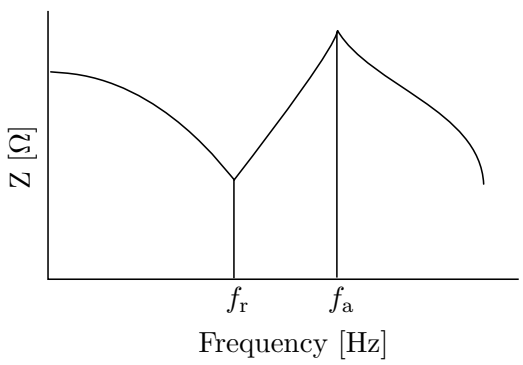

Figure 2.6: Impedance as a function of frequency.

A lumped-parameter equivalent circuit is shown in Fig. 2.5. The impedance as a function of frequency is shown in Fig. 2.6. Frequency f_r is the resonance frequency and f_a is antiresonance frequency. Resonance frequency depends on the piezoceramics used and on the shape and dimensions of the ceramics. There are usually three frequency constants that are given by piezoceramics manufacturers. They are defined:

$$N_\mathrm{P} = f_\mathrm{r} d \qquad \text{radial or planar} \tag{2.9a}$$

$$N_\mathrm{L} = f_\mathrm{r} l \qquad \text{longitudinal} \tag{2.9b}$$

$$N_\mathrm{T} = f_\mathrm{r} h \qquad \text{axial,} \tag{2.9c}$$

where d, l and h are diameter, length and thickness, respectively.

Aging rate

Aging rate is a logarithmic time dependence of the piezoelectric constants. The deterioration is given in percentage over time decade. Aging is caused by depolarization and by electro-mechanical fatigue.

Elastic constants and Young modulus

Either elastic constants or Young modulus appear in the piezo material documentation, since Young modulus is the reciprocal of elastic constants. Only constants in $_{33}$ and $_{11}$ directions are usually given.

Permittivity

Permittivity or dielectric constant is defined as electric displacement per unit electric field. Relative permittivity in $_{33}$ and $_{11}$ directions is usually given.

Curie temperature

It is a threshold temperature. When the material is above its Curie temperature it loses all remanent polarization. To regain the required piezoelectric abilities it has to be poled again.

Mechanical quality factor

Mechanical quality factor characterizes bandwidth relative to the center frequency. Higher mechanical quality factor means less damping and therefore piezoceramics with high mechanical quality factor are used for resonators.

Dielectric dissipation factor

Dielectric dissipation factor also called dielectric loss is defined as the ratio of effective series resistance to effective series reactance. It is given in percentage for oscillations at one kHz.

2.4.2 Nonlinear phenomena

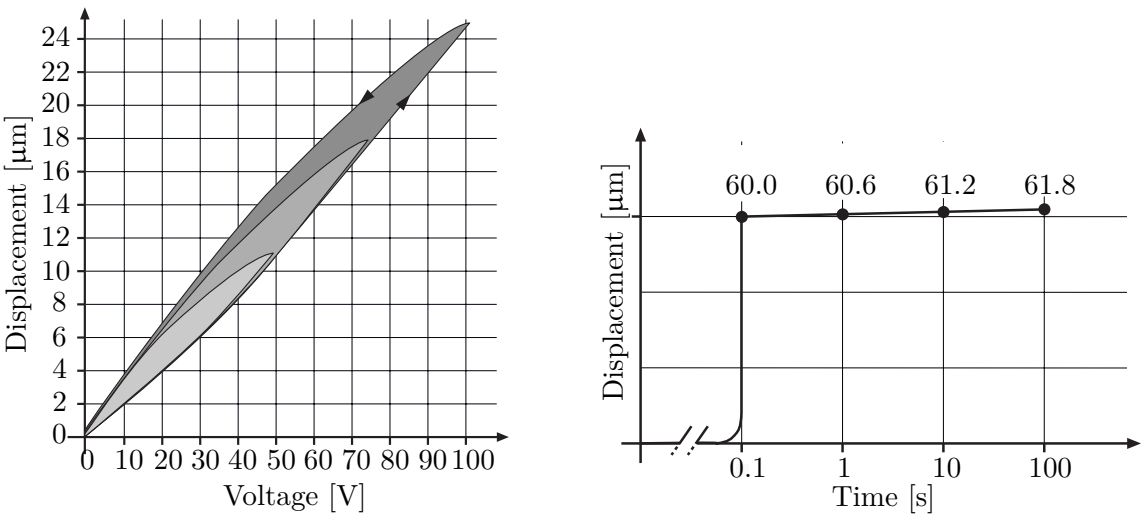

(a) Hysteresis **(b)** Creep

Figure 2.7: Nonlinear phenomena in piezo stack actuators [2].

Parameter	**Unit**	**PIC140**	**PIC255**	**BM532**	**APC855**
Density	g/cm^3	7.6	7.8	7.65	7.7
Curie temperature	°C	330	350	210	250
Coupling Factors	–				
k_p		0.5	0.62	0.65	0.68
k_{33}		0.6	0.35	0.75	0.76
k_{31}		0.325	0.69	0.39	0.40
k_{15}		-	-	-	0.66
Charge constants	10^{-12} m/V				
d_{33}		200	400	590	630
$-d_{31}$		60	180	270	276
d_{15}		265	560	-	720
Voltage constants	10^{-3} Vm/N				
g_{33}		28.2	25.1	20	21
$-g_{31}$		8.5	11.3	9	9
g_{15}		-	-	-	27
Elasticity	10^{-12} m^2/N				
s_{11}^E		11.7	16.1	14	16.9
s_{33}^E		11.7	20.7	20	19.6
Frequency constants	Hzm				
N_P		2200	2000	2000	1390
N_L		1680	1420	1425	2079
N_T		2100	2000	1850	1920
Relative permittivity	–				
e_{33}^σ/e_0		1200	1750	3250	3300
e_{11}^σ/e_0		680	-	-	-
Mechanical quality factor	–	350	80	70	65
Dielectric loss	%	1	1.5	2	1.3

Table 2.1: PZT ceramics parameters [2], [5], [6].

Hysteresis

The displacement of piezoceramics is not linearly dependent on voltage applied to the material as described in the IEEE Standard on piezoelectricity [4]. There is a hysteresis due to the repolarization of the domains during the operation. Hysteresis is observed to be rate-dependent, hysteresis is stronger for higher rate inputs. Experiments proved that hysteresis can be significantly suppressed by using current control and virtually removed by utilizing charge control. However, charge control has its disadvantages. This topic is discussed for instance in [7, 8]. See Fig. 2.7a.

Creep

Creep is another nonlinearity caused by changes of polarization in material. Creep is a slow increase in displacement in the direction of previously applied voltage even after it is no longer applied. The creep changes logarithmically in time and can add-up several % of the displacement step over a few hours. See Fig. 2.7b.

Temperature dependence

Apart from the thermal expansion there is a temperature dependence of piezoelectric constants on temperature. It can't be generally described for all the piezoceramics. Manufacturers often supply temperature dependence charts of their materials.

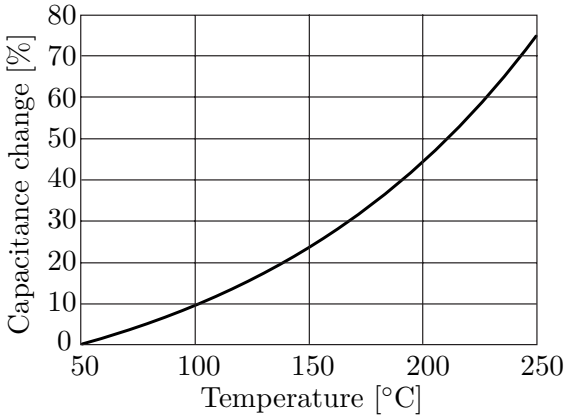

Figure 2.8: Capacitance as a function of temperature for PIC300 piezoceramics by PI [2].

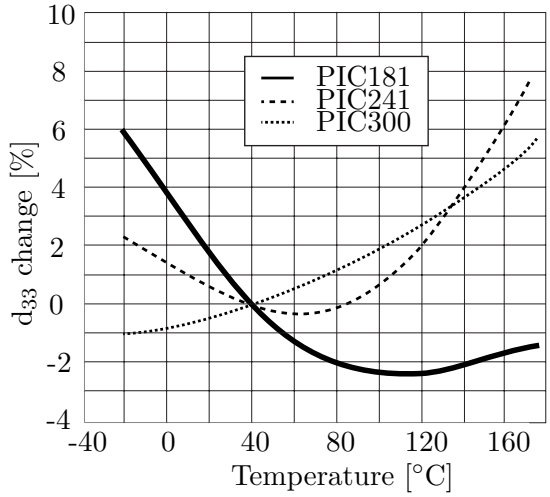

Figure 2.9: Charge constant d_{33} as a function of temperature for piezoceramics by PI [2].

Chapter 3

Piezoelectric actuators

This chapter gives a brief overview of piezoelectric actuators, while the main attention is focused on two actuator types, namely, stack actuators and ultrasonic plate actuators. Physik Instrumente's PI-840.1 stack and M-661 ultrasonic plate actuators, the main subjects of this project's experimental work, are introduced and the principle of their operation is explained.

3.1 Introduction

Piezoelectricity began to be practically utilized in 1910's-20's, mainly for sensors, measurement applications, sound-making and sound-capturing devices such as microphones, phones etc. [9]. Evolution of piezo actuators sped up in 1950's, when lead zirconate titanate (PZT) was developed [10]. According to [11], the first mass-production application of piezoelectric actuators was in dot-matrix printer by NEC in 1980's.

Piezoceramics is now the most important material for production of microactuators and micromanipulators, where piezo actuators replaced electromagnetic motors. Piezoelectric actuators do not create magnetic fields, they are smaller, have faster response time, there is no backlash or static friction and finally they require less power.

There are many types of piezoelectric actuators. They are most often divided according to the shape of PZT used. The shape determines the utilized piezoelectric constants. In other words the shape determines the vibration mode of the material that is used for actuation. We can find for example stripe, ring, tube and shear actuators. To strengthen the piezoelectric effect we can create actuators of various shapes with multiple layers of piezoceramics. All these actuators have one thing in common, the way they react to an input. As long as input voltage is applied, there is a strain. On the other hand there is a group of so called ultrasonic piezoelectric actuators or motors. These actuators require alternating input, each period of input creates a deformation in the ceramic that pushes the driven object one step further.

3.2 Stack actuator

3.2.1 Description

Single layer of piezoceramics is often not capable to produce sufficient displacements for reasonable voltage input. A greater thickness as well as input voltage is required to achieve

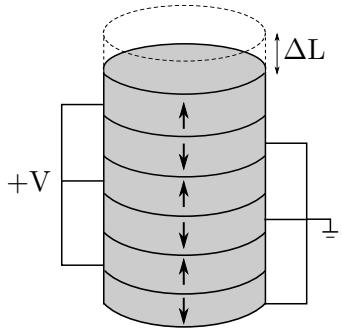

Figure 3.1: Piezo stack actuator, arrows mark the direction of layer polarization.

greater displacements. This problem can be solved by stacking multiple layers together. Stack actuator comprises multiple layers of piezoceramics divided by electrodes. Layers are most often disk-shaped, but ring or rectangular shaped are also manufactured. Layers are polarized along their thickness and the axis of motion, therefore the strain of the piezoceramics is dependent on d_{33} charge constant. A drawing of piezo stack actuator is shown in Fig 3.1. Stack actuators can be divided according to the input voltage to low-voltage and high-voltage actuators. The actuators of the first category are generally manufactured with layers between 25 µm to 100 µm in thickness and are driven with maximum input voltage between 100 to 200 V. The high-voltage stack actuators with maximum input of 200 to 1000 V have layer thickness between 400 µm to 1000 µm. Stack actuators can be operated in three modes - unipolar, semi-bipolar and bipolar. Unipolar operation expects input of one polarity, semi-bipolar usually allows opposite polarity input of up to 20% of the maximum positive voltage input, but the value depends on the manufacturer. These two modes can be used at room temperature. Bipolar operation is available just for a fraction of piezo stack actuators and usually requires lower-than-room temperature. The stack actuators are very sensitive to the orientation of load forces, they exhibit the best behavior when the load is along the axis of motion. Operation with load force vector deviation may damage the device or shorten its lifetime. Stack actuators are mainly used for pushing, they are very sensitive to tensile forces. To allow pulling, a preload in a form of low-stiffness spring must be applied. To improve durability and endurance to environmental conditions the stack is often placed in a steel casing. This also allows selling the stack actuators already preloaded, since the spring can be easily attached to the steel casing.

3.2.2 Actuator parameters

There are several parameters that manufacturers specify for their stack actuators. The nominal displacement range and voltage input range of the piezo stack actuators on the market is between 3 to 300 µm and −200 V to 1000 V, respectively. Length of the stack is usually 9 to 130 mm and operating temperature -20 to 80 °C for low voltage actuators and up to 200 °C for high-voltage ones. There are also actuators intended for cryogenic operating conditions, usually with bipolar voltage input.

Stiffness, blocking force and resonance frequency

Stiffness is an important parameter that allows computation of forces and resonant frequencies. Stiffness is different for open circuit and short circuit operation, it is different

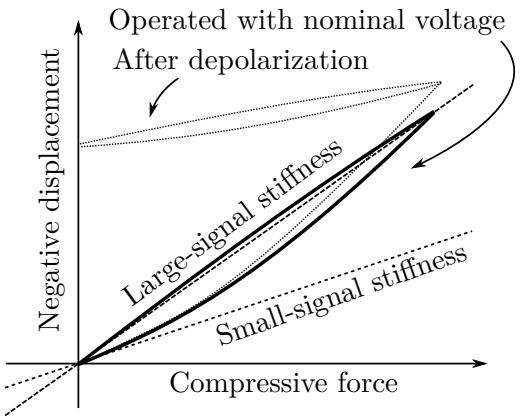

Figure 3.2: Quasi-static stiffness characteristic of piezo stack actuator [2].

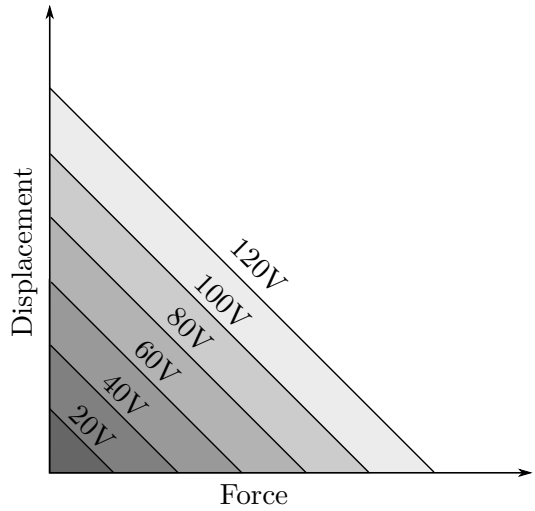

Figure 3.3: Piezo stack actuator working characteristic [2].

for small-signal and large-signal models and there is also a difference between static and dynamic stiffness. There is no standard for measuring stiffness, it is therefore incomparable between actuator manufacturers without additional explanation. The stiffness for various conditions is is shown in Fig. 3.2. Let's consider stiffness defined by eq. 3.1.

$$k_{\mathrm{T}} = \frac{F_{\mathrm{B}}}{\Delta L}, \tag{3.1}$$

where F_{B} is a blocking force, the maximum force the actuator can exhibit when no displacement is allowed, ΔL is the maximum displacement of the actuator, when no force is applied. The linear dependence between strain and force is shown in Fig. 3.3. Each line represents a set of operational points for one voltage level, i.e. possible values of force and displacement when certain voltage is applied.

Blocking force of stack actuators is usually between 1 to 80 kN. The stiffness values rise from several dozens up to 1800 N/μm for high voltage actuators, 10 to 500 N/μm for low voltage stacks. Stiffness increases with piezo layer diameter, decreases with actuator length, i.e. number of layers.

The resonance frequency is described by following equation:

$$f_{\mathrm{r}} = \frac{1}{2\pi}\sqrt{\frac{k_{\mathrm{T}}}{m_{\mathrm{eff}}}}, \tag{3.2}$$

where m_{eff} is an effective mass, which is one third of the piezo stack mass together with additional mass connected to the actuator. Stack actuators should operate at non-resonance frequencies, it is therefore recommended to choose actuator with resonance frequency at least two times the intended operational frequency. Resonance frequency decreases with length of the actuator, therefore for better dynamic properties, shorter stacks are better. The resonance frequencies are ordinarily between 5 to 60 kHz.

Electrical capacitance and amplifier requirements

Small-signal capacitance is defined as

$$C = n\varepsilon_{33}\frac{A}{t}, \tag{3.3}$$

where n is the number of layers, t is the layer thickness, A is the surface area of the piezoceramics layer and ε_{33} is the permittivity along the movement and polarization axis. The capacitance of piezo actuators generally depends on voltage, temperature and load and is generally quite complex. It is usually between 20 to 20000 nF. The capacitance as defined by eq. 3.3 is used to compute power or current required by the actuator to determine specifications of the piezo amplifier:

$$i_{\max} = f_{\max}\pi C U_{\mathrm{pp}}, \tag{3.4}$$

where $i_{\max}$ is the maximum current drawn by the actuator, $f_{\max}$ is the maximum application frequency, U_{pp} is a peak to peak input voltage.

Physik instrumente specifies a Dynamic Operating Current Coefficient (DOCC), which enables quick computation of maximum input current based on the application frequency and displacement. It is given in $\mu\mathrm{A/Hz}\cdot\mu\mathrm{m}$.

3.2.3 Physik Instrumente P-840.1

Leading German piezo devices manufacturer Physik Instrumente offers wide variety of stack actuators. From the cheapest ones without the steel casing to the most expansive embedded in the casing with preload and integrated encoder. P-840.1 is the smallest model of the preloaded in-casing, no-encoder series. Its parameters are summarized in Table 3.1.

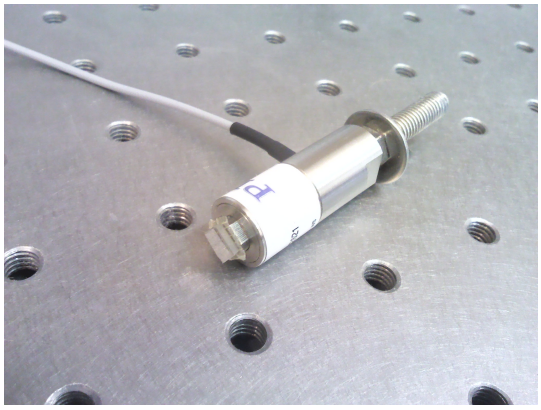

Figure 3.4: PI P-840.1 stack actuator.

Parameter	Value	Unit
max. displacement	15	µm
input voltage	0 – 100	V
max. push force	1000	N
max. pull force	50	N
stiffness	57	N/µm
capacitance	1.5	µF
DOCC	12.5	$\frac{\mu\mathrm{A}}{\mathrm{Hz}\cdot\mu\mathrm{m}}$
resonant frequency	18	kHz
length	32	mm

Table 3.1: P-840.1 datasheet parameters [2].

3.3 Ultrasonic motors

Ultrasonic motors is a very sizable group of piezoelectric actuating devices. There are two major groups of ultrasonic motors – traveling wave and standing wave ultrasonic motors.

The **traveling wave motors** have several electrodes placed on a piezoceramic ring, which together with elastic body forms a stator. The electrodes are excited by two-phase AC voltage signal with 90° phase difference. Each of the phases creates a standing wave in the stator. By superposition of both standing waves a traveling wave is created and the stator propels the rotor through frictional contact and a rotational movement is created. The contact points of stator follow elliptical trajectories in direction opposite to the rotor movement. This is depicted in Fig. 3.5.

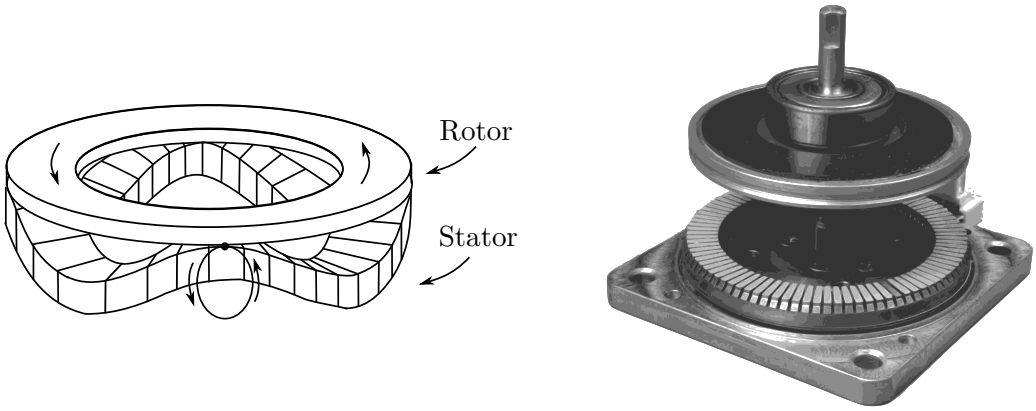

Figure 3.5: Traveling wave ultrasonic motor [12, 13].

Standing wave motors usually comprise a piezoceramic element with several electrodes attached [12,14,15]. The input to the actuator is AC voltage at resonance frequency of required vibrational modes of the piezoceramics element, that is usually between 20 kHz to 10 MHz. Two standing waves of the same frequency are created in the piezo element – one vibrating along the direction of motion and one perpendicular to it. This is depicted in Fig. 3.6. There is ideally a phase difference of 90° between the waves. This makes the friction point attached to the element follow an elliptical trajectory, as is shown in Fig. 3.7. The friction point is usually preloaded against the driven object and maintains friction throughout whole period. The normal force governing the frictional contact is higher when the friction point slides in the desired direction and lower when it slides in the opposite direction; consequently the motion is created by repeated poking of the friction point to the driven object. To change the direction of motion the phase difference of the input is switched to 270°. Amplitude of the input voltage affects the magnitude of vibration in the element and consequently its velocity.

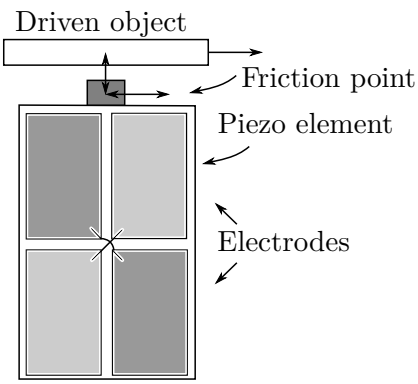

Figure 3.6: Possible configuration of standing wave ultrasonic motor [14].

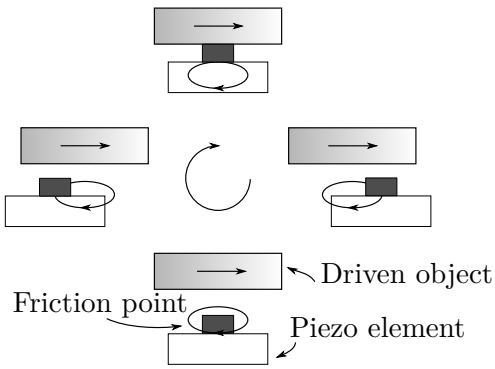

Figure 3.7: Elliptical trajectory of a standing wave motor's friction point.

3.3.1 Physik Instrumente M-661 ultrasonic linear plate actuator

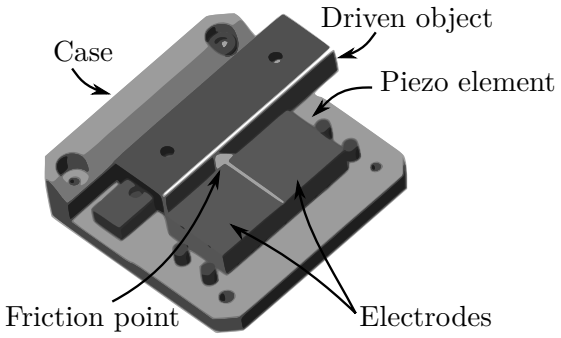

Figure 3.8: Ultrasonic linear plate actuator [2].

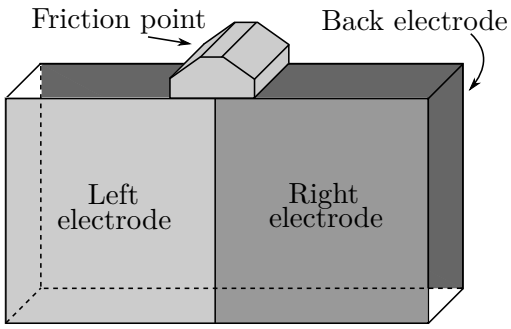

Figure 3.9: Piezoceramic element of the ultrasonic plate actuator in one of the possible electrode configurations.

This actuator belongs to the category of standing wave ultrasonic motors, but its operation is slightly different compared to the one described above. The following text is based on journal article by A. Vyshnevsky [16]. The heart of the actuator is a rectangular piezoceramics element, a plate, built into a metallic case as is shown in Fig. 3.8. The element is polarized along its thickness, which is much smaller than other dimensions. There are three electrodes in total placed on the large surface sides of the element, as is depicted in Fig. 3.9. The actuator is equipped with LEMO connector expecting a three-wire voltage input with each wire connected to one electrode. During the operation only one of the front electrodes is excited, thus applying asymmetrical electric field that causes asymmetrical vibration in the element and consequently a linear trajectory movement of the friction point. To change the direction of movement the other front electrode is excited and the first one is left to float. Physik Instrumente offers a variety of driver electronics that transform simple single-wire user control input to the three-wire one required by the actuator. Driver electronics used is discussed in Chapter 4.

Figure 3.10: Physik Instrumente M-661 ultrasonic plate actuator.

Parameter	Value	Unit
travel range	18	mm
min. step	50	nm
max. velocity	500	mm/s
max. load	5	N
max. push/pull force	1	N
max. holding force	2	N
operating voltage	120 (p-p) 42 (RMS)	V V
electrical power	5	W
max. current	400	mA
resonant frequency	215	kHz
dimensions	$30 \times 23 \times 10$	mm
mass	30	g
op. temperatures	-20 to 50	°C

Table 3.2: M-661 datasheet parameters [2].

Chapter 4

Instrumentation

4.1 Driver electronics for M-661 ultrasonic actuator

Physik Instrumente offers several driver electronics products. They are either for analog or PWM inputs, they differ in bandwidth size and come either as bare circuit boards with solder holes (C-184.161) or, in case of the more expensive ones, they have connectors instead and the high-end models are further encased in a metallic box. The C-184.161 driver electronics were chosen for driving the M-661 ultrasonic actuator. It transforms analog input voltage in the range of −10 to 10 V to the three-wire signal required by the actuator. Amplitude of the input controls velocity, polarity determines direction. This model is supplied by +12 V DC voltage. It is possible to fine-tune the output frequency of the driver by adjusting on-board potentiometer to match it as closely as possible to the resonant frequency of the particular actuator model to ensure the best working conditions.

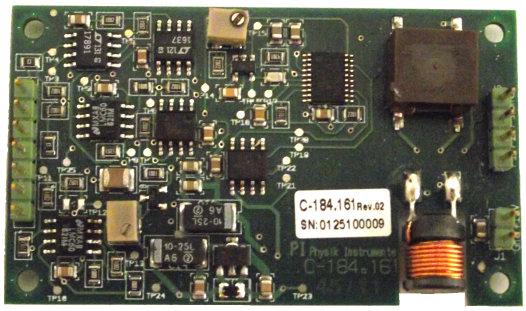

Figure 4.1: C-184.161 driver electronics by Physik Instrumente.

Parameter	Value	Unit
operating voltage	12	V
output power	5	W
output voltage	120 (p-p) 42 (RMS)	V V
current	400	mA
dimensions	65 × 38	mm
mass	15	g
op. temperatures	5 to 40	°C

Table 4.1: C-184.161 datasheet parameters [2].

4.2 Interferometer

4.2.1 Introduction

Interferometer is an optical measuring device, which utilizes optical interference between two light beams to measure relative displacement. There are many types of interferometers such as Fabry-Pérot, Sagnac, Mach–Zehnder, Michelson and many more [17]. Probably the most famous one is the Michelson interferometer, which is a predecessor of many

interferometers including those manufactured nowadays by SIOS Meßtechnik. Working principle of modified Michelson interferometer is explained on the following lines.

Working principle

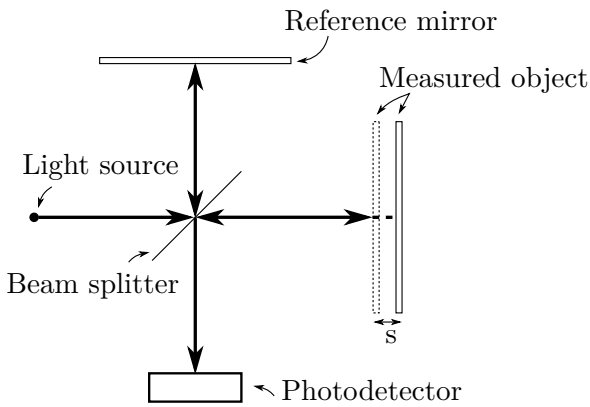

Figure 4.2: Modified Michelson interferometer.

A beam from a monochromatic (one-frequency) He-Ne laser splits on a beam splitter (e.g. a half silvered mirror or a beam-splitting cube). One of the beams follows a reference path, the other follows a path to the measured object. The beams are then reflected by plane mirrors back to the beam splitter, where they interfere. The interference is observed by a detector. See Fig. 4.2. We can look at the beams as planar monochromatic, linearly polarized waves. If the waves have phase difference of a wavelength multiple, they exhibit constructive interference, i.e. the amplitudes of the waves add-up to create a wave with greater amplitude. If the waves have a phase-difference of odd multiple of half a wavelength, they exhibit a destructive interference, the waves cancel each other. To determine the interference we can measure the intensity of the resultant wave by photodetectors.

Lets assume the measured object changes its displacement by s. The intensity of the wave at the photodetector is described by eq. 4.1.

$$\begin{aligned} I &= I_1 + I_2 + 2\sqrt{I_1 I_2}\cos(\gamma + \gamma_\mathrm{M}), \\ \gamma_\mathrm{M} &= \frac{2\pi}{\lambda_0} n\, i\, s, \end{aligned} \tag{4.1}$$

where I_1 and I_2 are the intensities of interfering waves, γ describes the interference pattern before the displacement, γ_M describes the phase change after the displacement, λ_0 is a wavelength, n is a refractive index of air and $i = 2$ is an interferometer factor. For the displacement we can write

$$s = \frac{k\lambda_0}{i\,n} = \frac{k\,c_0}{i\,n\,f_\mathrm{HeNe}}, \tag{4.2}$$

where c_0 is the speed of light, f_HeNe is a frequency of the laser, k is an interference order, i.e. the number of wavelengths. We can determine the smallest measurable displacement:

$$s = \frac{\lambda_0}{e\,i\,n}, \tag{4.3}$$

where e is the number of electronic increments per interference order. The equations were taken from [18].

Interferometers can measure in sub-wavelength resolution, depending on the photodetector sensitivity to intensity of light. The resolution is further limited by other factors such as instability of the laser, dependence of the refractive index of air on the air humidity, pressure and temperature or instability of the measured object.

4.2.2 SIOS SP 2000-TR

Figure 4.3: SIOS SP 2000-TR power-supply/signal-processing unit.

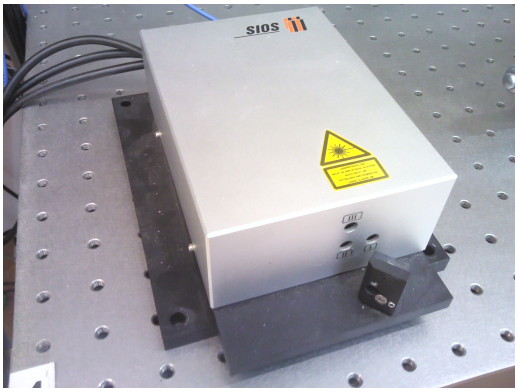

Figure 4.4: SIOS SP 2000-TR sensor head.

Description

SIOS SP 2000-TR is a plane-mirror triple-beam interferometer. The three beams supplied by one frequency stabilized He-Ne laser at 632.8 nm wavelength allow three-axial measurement. The whole measurement set comprises not only the interferometer, but also temperature, pressure and humidity sensors for computing Edlén correction of the refractive index of air. The interferometer head shown in Fig. 4.4 and all the sensors are connected to power-supply/signal-processing unit, see Fig. 4.3. The unit consists of several euro-card format circuit boards (modules) in 19-inch rack-mount chassis. The design is modular, allowing the customer to choose the modules he needs. The interferometer available at the Department of Control Engineering comprises following modules: power supply, laser output, external clock, environmental control module and three modules for each channel – a signal processing, digital controller and optoelectronic modules.

Apart from the laser source, the core interferometer described in the previous section is embedded in the sensor head. The laser beam is brought by a single-mode optical fiber. The measured data of each of the channels is transferred to the optoelectronic EM-10 module, where it is amplified and offset corrected. Digital controller module RG-10 works as a signal feedback. It takes the output of EM-10 and computes gain and offset parameters to be set by EM-10. RG-10 is also used for calibration of the sensor head as described later. The signal-processing module RE-06 takes the output of the optoelectronic module and converts it to digital signal using its 8-bit flash converters. It computes the angles and through an arctangent decoding table the displacements. The data is send to the PC via USB or RS-232.

The SIOS SP 2000-TR interferometer works with 1 nm resolution over the range of 2000 mm with maximum measured object translation rate of 800 mm/s.

Calibration

The aim of the calibration is to tune the interferometer electronics and optics to produce signals that can be decoded to displacement values. First of all the laser beam leaving the sensor head must be reflected from the measured object back to the aperture. The measured object has to be able to reflect the beam. This can be taken care of by attaching e.g. a plane mirror. We can start by roughly aligning the sensor head and the measured object. With a piece of white paper we can track the reflection (a red dot) on the sensor head and by fine tuning either the fixture the sensor head is placed on, or by tweaking the measured object alignment, we can move the reflection to merge with the original beam leaving the interferometer. To allow calibration the signal sensor head is equipped with piezoelectric transducer that moves with the reference mirror, see Fig. 4.2. That causes the interference and therefore the intensity at the photodetectors to periodically change. There are two photodetectors, the interference beam is split into two beams, one for each photodetector. The reason for this is to allow directional measurement, which would not be possible with just one photodetector. The output of the photodetectors are sine and cosine differential signals that are after amplification and offset correction available through BNC connectors of EM-10 optoelectronic module for calibration. The signals should be for calibration purposes connected to oscilloscope and displayed in XY mode. The signals of desired phase and amplitude create a Lissajous figure of thin closed circle. By fine tuning the alignment of the sensor head and measured object and by creating the Lissajous circle we ensure that the interference fringes are correctly read and that the signals are in shape for displacement decoding. Due to the aging and mechanical fatigue of the piezotransducer, the vibrations frequency and amplitude change with time. These parameters can be adjusted through RG-10 module. This helps in closing a disconnected Lissajous circle if aligning the measured object does not suffice. For actual measurement the piezoelectric transducer is turned off, the reference mirror is in a still position and the interference is created just by the movement of the measured object.

Measurement settings

SIOS Meßtechnik provides two means of interaction with interferometer via PC. One is through INFAS software and the other through *siosusb* library, which is described in detail in Appendix A. There are three modes for measurement – normal, fast and superfast. In normal mode interferometer measures and processes data with sampling frequency of primary values of up to 16 kHz. The primary values can be averaged and/or filtered with the downside of lowering maximum sampling rate. The data is send at request through USB or RS-232 bus. Since the communication with interferometer is not fast enough the sampling rate is further limited. Faster sampling rates are achievable in fast mode. It does not allow continuous reading of measured data, it stores the data in a built-in RAM and sends them to PC when the measurement is finished. Superfast mode uses direct memory access to store the data in the internal RAM and offers even higher sampling rates – up to 1 MHz. Both fast and superfast modes support using a trigger input to start a measurement. Triggering each data value is possible only in fast mode. The downside of the latter two modes is the RAM capacity. The interferometer available can store up to 32768 data values, which limits the time window when measuring at the maximum frequency to ≈ 33 ms.

Chapter 5

Modeling stack actuator

During the last two decades there have been many stack actuator models developed for various applications. The simplest ones are linear, based on the constitutive equations given by the IEEE Standard on Piezoelectricity [4]. These models are used in less accurate applications such as active vibration control. For higher accuracy applications, nonlinearities such as hysteresis and creep must be included. Hysteresis could be modeled as rate-independent phenomenon, but since it is often observed to be highly rate-dependent, the highest precision applications require incorporating rate-dependent models.

In this chapter two models of piezoelectric stack actuators are presented, the Nonlinear lumped parameter model and the General bond graph model. The second part of the chapter introduces three hysteresis models – Al Janaideh's Prandtl–Ishlinskii model, Ang's Prandtl–Ishlinskii model and Maxwell resistive capacitor model. Simulations and measurements are discussed in Chapter 6.

5.1 Stack actuator models

On the following lines two models, that stand out from the rest, are described. The *Nonlinear lumped-parameter model* – a classical model for piezo actuators in general is here used to describe stack actuator. The sources of information for developing this model are journal articles written by M. Goldfarb [19] and M. Quant [20]. The second model is a modification and a generalization of the first model, so called *General bond graph model*, by J. M. Rodriguez–Fortun [21].

5.1.1 Nonlinear lumped-parameter model

This model considers two domains as is shown in Fig. 5.1 – electrical and mechanical. Input voltage applied to the actuator, denoted as V_{in}, is split into V_{h}, voltage over hysteresis element H and V_{t}, voltage over a capacitor representing the capacitance of the actuator. V_{t} is transformed to a force F through a electro-mechanical constant T. The mechanical part is modeled as a simple mass-spring-damper system with mass m, stiffness k and damping b. The displacement of the actuator, charge in the piezoceramics and external forces are denoted by x, q and F_{e}, respectively. We can rewrite the model into mathematical equations:

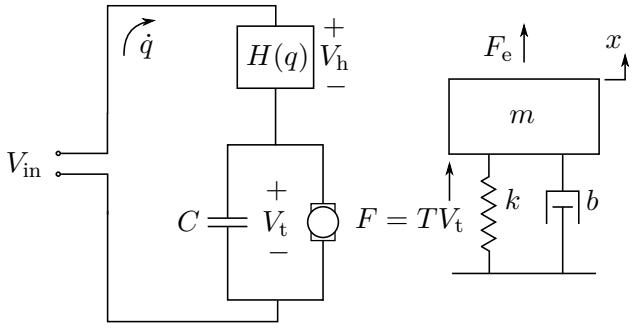

Figure 5.1: The Nonlinear lumped parameter model. Drawing inspired by [19] and [20].

$$
\begin{aligned}
V_{\text{in}} &= V_{\text{h}} + V_{\text{t}}, & F &= TV_{\text{t}}, \\
V_{\text{h}} &= H(q), & F + F_e &= m\ddot{x} + b\dot{x} + kx. \\
q &= Tx + CV_{\text{t}}
\end{aligned}
\tag{5.1}
$$

5.1.2 General bond graph model

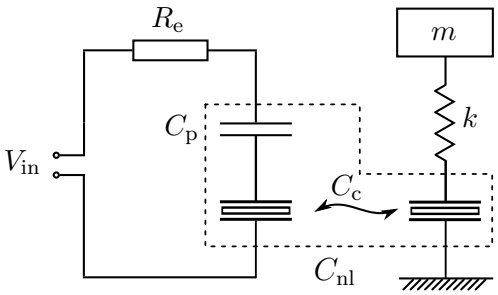

Figure 5.2: A model of piezoceramics layer - a basis for creating the General bond graph model. Drawing inspired by [21].

Bond graph modeling, invented by H. Paynter in late 50's at MIT is a graphical modeling technique, which focuses on the power flow in the system, possibly through various domains. There are three domains considered in Rodriguez–Fortun's *General bond graph model*. The macroscopic electrical and mechanical domains are connected through a 'polarization' domain. To model the stack actuator, we can assume that all layers it comprises have the same properties and thus we can consider model of the piezoceramic layer depicted in Fig. 5.2 to represent whole piezoelectric stack. The energy accumulating elements C_c and C_p can be joined to one denoted C_{nl}. C_p represents the capacitance of the piezoceramics and C_c represents nonlinear energy accumulating coupling between electrical and mechanical domains of the piezo material.

The bond graph based on this model is shown in Fig. 5.3. Small arrows at the end of each power bond show a direction of positive power flow. The power at each bond is given by the product of the two quantities shown next to the bond. For example in electrical domain power is a product of voltage and current, in mechanical domain it is a product of force and velocity. Small strokes perpendicular to a bond denote causality, i.e. which of the two quantities is the input and which the output. There are two energy accumulating elements – inertances and compliances. Inertance represents mass in

mechanical and inductance in electrical systems. Compliance represents a reciprocal of spring stiffness in mechanical and capacitance in electrical systems. Compliance C_{nl} is placed in a 'polarization domain'. Its modulus is defined:

$$C_{\mathrm{nl}} = \frac{p}{E} \left[\frac{\mathrm{Cm}^2}{\mathrm{V}}\right], \tag{5.2}$$

where p is electric dipole and E is electric field. Much more information about bond graphs can be found in [22].

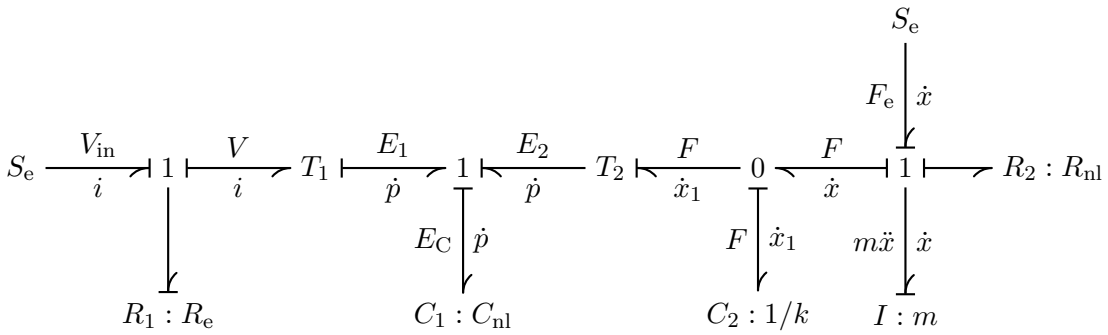

Figure 5.3: General bond graph model of piezo stack actuator.

Let's look at the bond graph from the left hand side and follow in the direction of positive power flow. The input voltage V_{in} diminished by input resistance R_{e} is transformed to electric field E_1, while the current drawn is transformed to a derivative of electric dipole p. This is in the bond graph represented by transformer T_1. Since it is an ideal transformer, the power on both sides is conserved. External forces F_{e}, mass m, stiffness k and a nonlinear damping R_{nl} on the right hand side of the bond graph form a mass-spring-damper system with force output F, which is transformed by an ideal transformer T_2 to electric field E_2. The energy is then stored in compliance C_{nl}, which includes linear capacitance of the piezoceramics and a hysteresis model, which makes C_{nl} nonlinear function of p. We can rewrite it to the following mathematical equations:

$$\begin{aligned} V &= V_{\mathrm{in}} - R_{\mathrm{e}} i, & E_{\mathrm{C}} &= C_{\mathrm{nl}}(p), \\ E_1 &= \frac{V}{\ell}, & E_2 &= F\frac{T}{\ell}, \\ \dot{p} &= i\ell, & F &= k(x - x_1), \\ E_{\mathrm{C}} &= E_1 - E_2, & F_{\mathrm{e}} &= m\ddot{x} + R_{\mathrm{nl}}\dot{x} + F, \end{aligned} \tag{5.3}$$

where i denotes a current, ℓ is a length of stack and T is an electro-mechanical constant. A state space model can be derived directly from the bond graph:

$$\begin{aligned} \frac{\mathrm{d}p}{\mathrm{d}t} &= \frac{\ell}{R_{\mathrm{e}}}(V_{\mathrm{in}} - E_{\mathrm{C}}(p)\ell + kTx_1), & \frac{\mathrm{d}v}{\mathrm{d}t} &= -\frac{1}{m}(kx_1 + R_{\mathrm{nl}}v), \\ \frac{\mathrm{d}x_1}{\mathrm{d}t} &= v - \frac{T}{R_{\mathrm{e}}}(V_{\mathrm{in}} - E_{\mathrm{C}}(p)\ell + kTx_1), & \frac{\mathrm{d}x}{\mathrm{d}t} &= v. \end{aligned} \tag{5.4}$$

5.2 Hysteresis models

Hysteresis modeling in piezoelectric actuators has been a very popular research topic over the last decade. There are many methods and approaches available. We can divide them

to those that are based on the physical description of hysteresis and to those that are not, often referred to as phenomenological models. Majority of hysteresis models belong to the latter category. Many phenomenological hysteresis models are based on mathematical operators, such as Preisach, Krasnosel'ski–Pokrovski, Maxwell resisitive capacitor and Prandtl–Ishlinskii models. Bouc–Wen model and its variations is an example of a well-known phenomenological model that is not based on mathematical operators.

Prandtl–Ishlinskii has been the most popular model recently. The main reason for its popularity is it's analytical invertibility, which is discussed later in Chapter 7. In this chapter three rate-independent hysteresis models are introduced – Maxwell resistive capacitor model and two variations of Prandtl–Ishlinskii model. Model simulations and laboratory experiments with real stack actuator are discussed and compared in Chapter 6.

5.2.1 Prandtl–Ishlinskii model

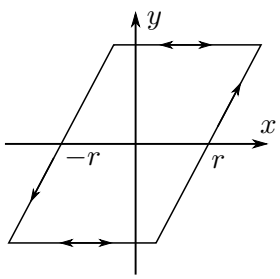

Figure 5.4: Backlash operator used in Prandtl–Ishlinskii model.

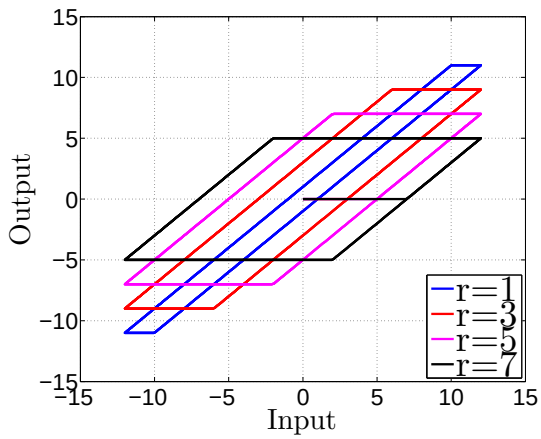

Figure 5.5: Output of backlash operators with different widths for input $12\sin(2\pi)$.

This model is based on *backlash* operators. Such an operator is shown in Fig 5.4. The following mathematical definition of backlash operator is taken from [23]:

$$\begin{aligned} y(t) &= F_r[x, y_0](t), \\ &= \max\big(x(t) - r, \min\big(x(t) + r, y(t - T)\big)\big), \\ y(0) &= \max\big(x(0) - r, \min\big(x(0) + r, y_0\big)\big), \end{aligned} \tag{5.5}$$

where x denotes input and y output, y_0 is the initial value, usually $y_0 = 0$. Parameter t is time and T is a discrete time step. We can obtain the Prandtl–Ishlinskii model by summation of outputs of several weighted operators with different operator widths r. Outputs of operators with equal weights and different widths are plotted in Fig. 5.5.

5.2.2 Al Janaideh's Prandtl–Ishlinskii model

The rate-independent model presented on the following lines is a combination of several models made by O. Al Janaideh and published in journal articles [24–27]. This symmetrical

model of hysteresis is defined by equation:

$$\Phi(x(t)) = q\eta(x(t)) + \sum_{j=1}^{J} \Theta_j F_{r_j}\Big(\eta(x(t))\Big), \tag{5.6}$$

where η is an envelope function of the operators and Θ is a density function. I have chosen the widths of the backlash operators r_j to be equidistant with interval σ_r:

$$r_j = j\sigma_r$$

and the envelope and density functions to be:

$$\begin{aligned} \eta(x(t)) &= cx(t), \\ \Theta_j &= \alpha e^{-\beta r_j}. \end{aligned}$$

The number of operators J is chosen experimentally to model the hysteresis with sufficient precision and manageable computational cost. From the set of parameters $\Omega = \{q, c, \sigma_r, \alpha, \beta\}$ we want to find such parameters Ω_{opt} that make the error $E(\Omega)$ between measured data $Y(i)$ and simulated data $\Phi(x(i), \Omega)$ minimal. We can write it mathematically:

$$\begin{aligned} E(\Omega) &= \sum_{i=1}^{I} \Big(\Phi(x(i), \Omega) - Y(i)\Big)^2, \\ \Omega_{\text{opt}} &= \arg\min_{\Omega} E(\Omega), \end{aligned} \tag{5.7}$$

where i denotes each of I data points.

5.2.3 Ang's Prandtl–Ishlinskii model

The following rate-independent Prandtl–Ishlinskii model, which is based on journal article written by Ang [23], uses two operators. To allow modeling asymmetrical hysteresis, one-sided deadzone operators are used together with backlash operators defined by eq. 5.5. One-sided deadzone operator is defined:

$$S_d[x](t) = \begin{cases} \max(x(t) - d, 0), & d > 0 \\ x(t), & d = 0 \end{cases}$$

where x is an input and d is operator width. This operator is depicted in Fig. 5.6.

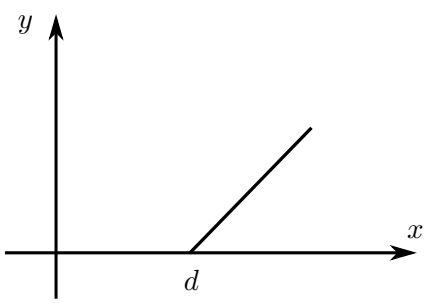

Figure 5.6: One-sided deadzone operator.

Ang's Prandtl–Ishlinskii model is defined

$$z(x,t) = \mathbf{w_s}^{\mathrm{T}}\mathbf{S_d}\big[\mathbf{w_f}^{\mathrm{T}}\mathbf{F_r}[x,\mathbf{y_0}]\big](t), \tag{5.8}$$

where

$$\mathbf{w_f}^{\mathrm{T}} = \big[w_{\mathrm{f}_0}, w_{\mathrm{f}_1}, \ldots, w_{\mathrm{f}_J}\big]$$

is the backlash operator weight vector. The vector of backlash operator is defined

$$\mathbf{F_r}[x](t) = \big[F_{r_0}[x](t), F_{r_1}[x](t), \ldots, F_{r_J}[x](t)\big]^{\mathrm{T}},$$

where J is the number of backlash operators used and

$$\begin{aligned} \mathbf{r} &= \big[r_0, \ldots, r_J\big], \\ &\big[0 = r_0 < \cdots < r_J\big]. \end{aligned}$$

Vector of one-sided deadzone operators and it's weight vector is defined

$$\begin{aligned} \mathbf{S_d}[x](t) &= \big[S_{d_0}[x](t), S_{d_1}[x](t), \ldots, S_{d_m}[x](t)\big]^{\mathrm{T}}, \\ \mathbf{w_s}^{\mathrm{T}} &= \big[w_{\mathrm{s}_0}, w_{\mathrm{s}_1}, \ldots, w_{\mathrm{s}_m}\big], \end{aligned}$$

where m is the number of deadzone operators used and

$$\begin{aligned} \mathbf{d} &= \big[d_0, \ldots, d_m\big], \\ &\big[0 = d_0 < r_J < d_1 \cdots < d_m\big]. \end{aligned}$$

Both backlash operator widths and deadzone operator widths are chosen to be equidistant, but only between $d_1, \ldots, d_m$ for the latter. The model is identified similarly to Al Janaideh's. A set of parameters Ω comprises:

$$\Omega = \{\mathbf{w}_{\mathrm{s}}, \mathbf{w}_{\mathrm{f}}, d_1, \sigma_d\}, \tag{5.9}$$

where σ_d is the interval between widths of deadzone operators. Note here that the backlash operator width interval is not included. The r_Jth operator width is set to equal half of the input range and thus the interval is determined by dividing this value by number of backlash operators.

$$\begin{aligned} E(\Omega) &= \sum_{i=1}^{I} \Big(z\big(x(i),\Omega\big) - Y(i)\Big)^2, \\ \Omega_{\mathrm{opt}} &= \arg\min_{\Omega} E(\Omega), \end{aligned} \tag{5.10}$$

where $z\big(x(i)\big)$ is output of the simulated model and $Y(i)$ measured output of stack actuator. i denotes each of I data points.

5.2.4 Maxwell resistive capacitor model

There are lots of similarities between Maxwell resistive capacitor hysteresis model and Prandtl–Ishlinskii models introduced earlier. This model is also composed of several hys-

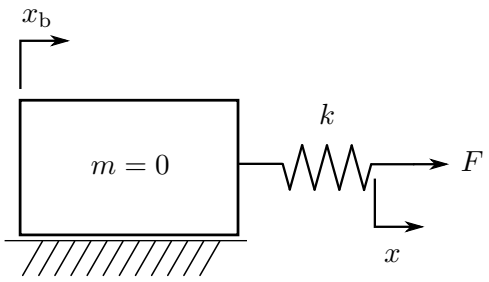

Figure 5.7: Elasto-slide element of the Generalized Maxwell slip model.

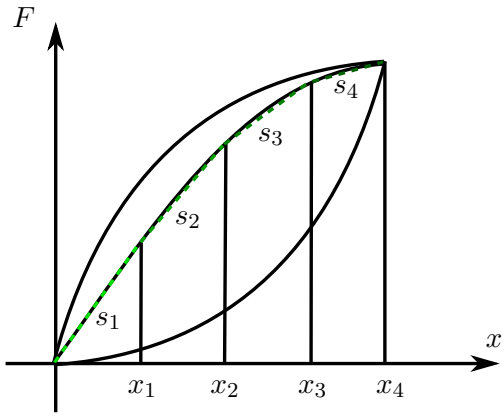

Figure 5.8: Hysteresis loop of the Generalized Maxwell slip model with piece-wise linear fit of the loading curve.

teresis operators, but not backlash operators as models above. The principle of this model can be explained from a electrical or mechanical viewpoint, we don't have to rely on pure mathematics. Let's look at the mechanical version of this model, called *Generalized Maxwell slip*, which is more intuitive to understand than its electrical counterpart. It models hysteresis between input displacement and output friction force. Each operator can be represented by an elasto-slide element shown in Fig. 5.7. There are two parameters considered for each element – stiffness of the spring k and a breakaway force f. The massless block is subject to Coulomb friction, i.e. until the applied force equals the breakaway force, the block does not move and the friction force equals the applied force. The force applied is given by the product of input displacement x and spring stiffness k. When the breakaway force is reached the friction force saturates and the block's position x_b changes. The following mathematical definition is taken from [19]:

$$F = \begin{cases} k(x - x_\mathrm{b}) & \text{if } |k(x - x_\mathrm{b})| < f \\ f \ \mathrm{sign}(\dot{x}) \text{ and } x_\mathrm{b} = x - \frac{f}{k}\mathrm{sgn}(\dot{x}) & \text{else,} \end{cases}$$

where F is the output friction force. The hysteresis is modeled by combining several of the elasto-slide elements in parallel, each with different parameters k and f. Sum of the friction forces of each element is the output of this model. Since the mass of the block is considered to be zero, having more of these elements does not increase order of the system, while improving accuracy and increasing computational demands.

Fig. 5.8 shows a hysteresis loop between displacement and force, which can be described by this model. Loading curve appears during the first half-period of harmonic input signal, before the hysteresis gets to a 'steady' loop. If there is no remanent hysteresis at the starting time, we can identify parameters of this hysteresis model by splitting the loading curve to n segments of equal length on the x axis, while n also denotes number of

elasto-slide elements of the resultant model. It has the following properties:

$$\begin{aligned} s_i &= \sum_{j=i}^{n} k_j, \\ f_i &= k_i x_i, \end{aligned} \tag{5.11}$$

where s_i is its slope at ith segment $\langle x_i, x_{i+1} \rangle$. Breakaway force f_i is a difference of the curve outputs at ith segment's end points. We can obtain the segment slopes $\mathbf{s}$ from piece-wise linear fit of the loading curve and the stiffness parameters for each elasto-slide element $\mathbf{k}$ from simple matrix multiplication

$$\mathbf{k} = \mathbf{A}^{-1}\mathbf{s}, \tag{5.12}$$

where $\mathbf{A}$ is an upper triangular matrix. We can obtain the vector of breakaway forces $\mathbf{f}$ from the following equation:

$$\mathbf{f} = \mathbf{K}\mathbf{x}, \tag{5.13}$$

where $\mathbf{K}$ is diagonal matrix of spring stiffnesses and $\mathbf{x}$ is a vector of segment locations.

Since this model is used in electrical domain between charge and voltage, we can simply substitute reciprocals of capacitances C_i for parameters k_i, change breakaway forces f_i to breakaway voltages v_i and consider charge q and q_b instead of displacements x and x_b, thus obtaining the Maxwell resistive capacitor hysteresis model.

Chapter 6

Simulations and measurements of stack actuator

In this chapter the models introduced in Chapter 5 are compared with a real piezo stack actuator PI-840.1 from Physik Instrumente presented in Chapter 1. After introducing the measurement setup and giving description of how to obtain mechanical parameters of the models, simulations of the hysteresis models are compared with interferometer measurements of the real stack actuator's displacement. Before discussion of problems encountered during the measurements, the final conclusion and evaluation of the experiments performed, two complete electro-mechanical models with hysteresis model included are presented together with the corresponding experimental results.

6.1 Measurement setup

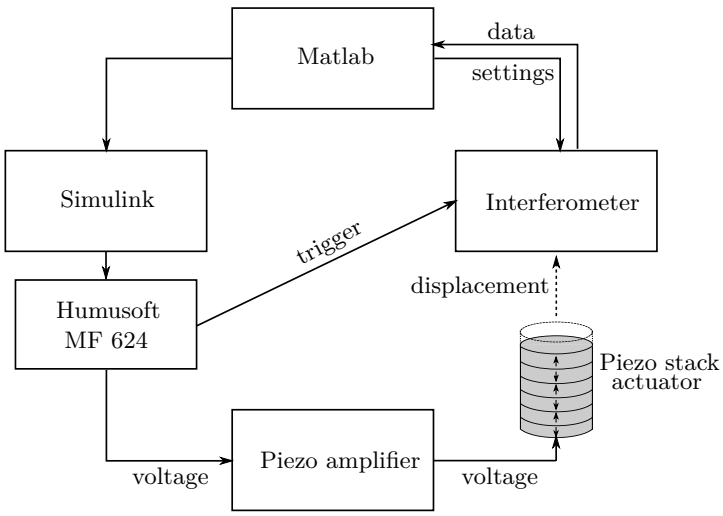

Figure 6.1: Measurement setup for piezo stack actuator.

The measurement is controlled by a PC running Matlab 2012b. Input signal is generated in Simulink and send through a Humusoft MF 624 card [28] to piezo amplifier EPA-104 [29] before getting to the piezo stack acutator. Together with actuator input a starting trigger pulse is send to the SIOS SP 2000-TR interferometer to start the measurement at the same time as the input enters the actuator. Interferometer is used in a

superfast mode, see Chapter 4 for details. Data length of 32768 data points was chosen with sampling frequency 3125 Hz, which gives us approximately 10.5 s measurement window. After the measurement, the interferometer sends the data from its internal memory directly to Matlab, where it is processed. Communication between the interferometer and PC is established through USB.

6.2 Mechanical parameters identification

Nonlinear lumped-parameter and General bond graph model have three parameters in common – mass m, stiffness k and electro-mechanical constant T. Mass and stiffness are available in the actuator's documentation [30]. However, mass is given as a 'mass without cables' and thus includes metal casing and possibly other objects. Since dismantling the piezo stack from the metal casing would irreparably damage the actuator, the value shown in Tables 6.1 and 6.2 is an educated guess of the weight of the piezoceramics. Stiffness given in the documentation is also not very reliable and based on the experiments higher value is used. The problems with stiffness are discussed in Chapter 3.

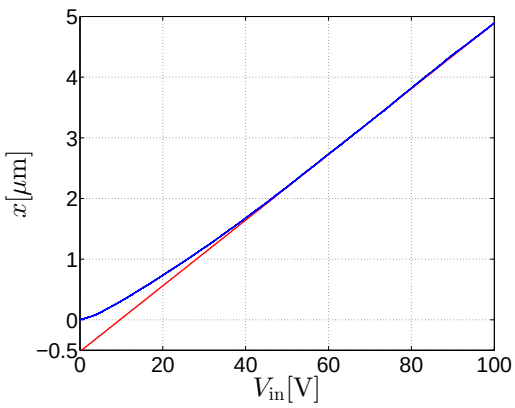

Figure 6.2: Loading curve (blue) used to determine electro-mechanical constant given by the slope of it's tangent (red) near maximum input voltage.

The electro-mechanical constant can be obtained by approximating the loading curve of the actuator. The idea presented by L. Juhász in [31] requires cleaning any remanent hysteresis by applying sine signal with zero mean and linearly decreasing amplitude. Due to the fact, that the stack actuator available is intended for unipolar operation only, the peak voltage of the decaying sinusoidal signal was chosen not to get lower than −20 V. The signal used is described by following equation:

$$V_{\text{in}} = (-7.5t + 20)\sin(2\pi 1.8t) \qquad \text{for } t \in \langle 0, 2.67 \rangle\,. \tag{6.1}$$

The loading curve is measured after application of linearly increasing input voltage in the range of 0–100 V within 10 s. The measured displacement is then plotted as a function of input voltage. The input voltage axis is then segmented into 50 equidistant parts and the points of the loading curve lying at the endpoints of the last segment are connected with a straight line. When input reaches its maximal value, the hysteresis should have minimal or no influence on the output displacement and therefore the slope of the line through the last segment can be considered equal to electro-mechanical constant of the model. The loading curve together with the line is shown in Fig. 6.2.

Nonlinear lumped-parameter model uses two more parameters – damping and capacitance. Damping has been obtained experimentally from the step response of the actuator. It is highly nonlinear and the value used is totally unreliable. Since damping as it turned out from the experiments is an unimportant parameter, knowing just its order is enough.

General bond graph model requires stack length l, area of piezoceramic layer perpendicular to the direction of polarization, denoted A, and electrical resistance R_e between amplifier and actuator. The first two parameters were computed from the information given in the actuator's documentation [30]. Simulations showed that changes over several magnitudes in R_e have virtually no effect on the output, thus the parameter was chosen randomly. The damping parameter R_nl was omitted.

Parameter	**Symbol**	**Value**	**Unit**
stiffness	k	65	N/µm
mass	m	16	g
damping	b	80	Ns/m
capacitance	C	1.5	µC/V
electro-mechanical constant	T	3.52	N/V

Table 6.1: Nonlinear lumped-parameter model parameters.

Parameter	**Symbol**	**Value**	**Unit**
stiffness	k	65	N/µm
mass	m	16	g
electro-mechanical constant	T	3.52	N/V
stack length	l	18	mm
layer area	A	1.13	cm^2
electrical resistance	R_e	5	Ω

Table 6.2: General bond graph model parameters.

6.3 Hysteresis

Hysteresis has a great influence on the behavior of stack actuators and Physik Instrumente's P-840.1 is no exception. Fig. 6.3 shows hysteresis loops for 2 Hz nominal sinusoidal and triangular input voltage. The loops are very similar, with the biggest difference at the edges of the input range. The loops have a maximum thickness of approximately 770 nm, which is nearly 16% of the maximum displacement of the actuator. Fig. 6.5 shows the same data as a function of time and the absolute error of the measurement is depicted in Fig. 6.6. Hysteresis is observed to be rate-dependent as is shown in Fig 6.4. We can see that the loop width doubles when 100 Hz sine input is used compared to the 2 Hz input. Also amplitude of the displacement is slightly lower at higher rates.

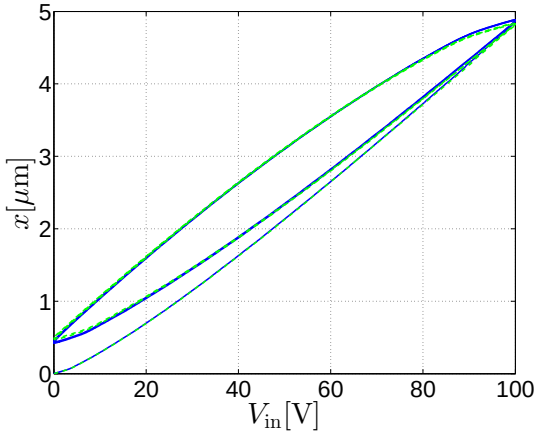

Figure 6.3: Hysteresis loops for 2 Hz sinusoidal (blue) and triangular (green) inputs.

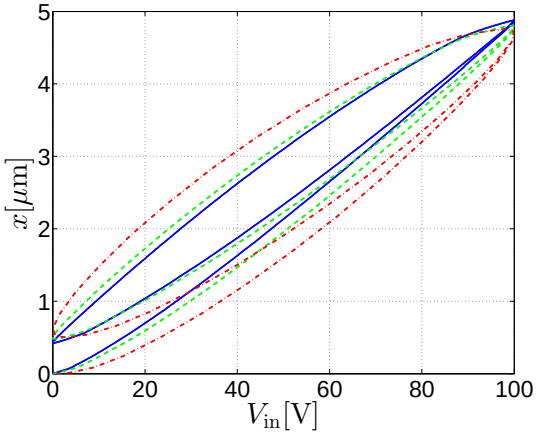

Figure 6.4: Hysteresis loops for sinusoidal inputs at 2 Hz (blue), 10 Hz (green) and 100 Hz (red).

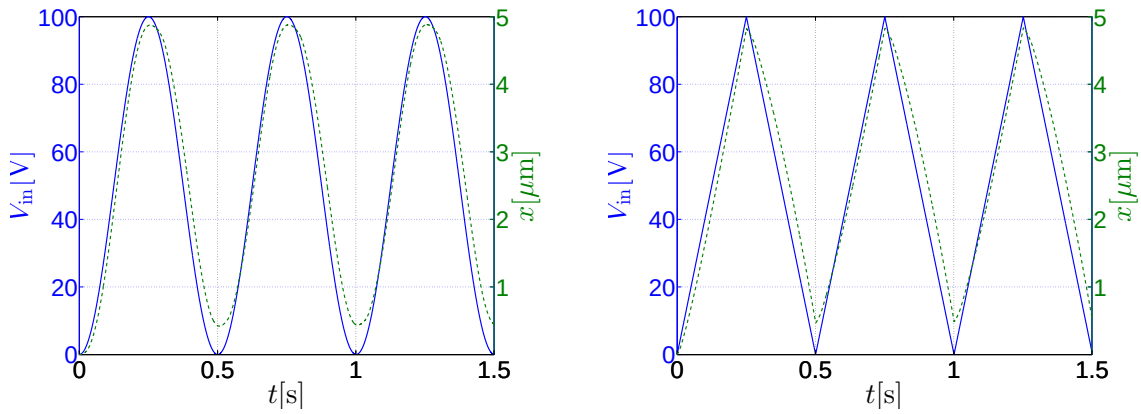

Figure 6.5: Measured displacement for sinusoidal and triangular voltage inputs at 2 Hz.

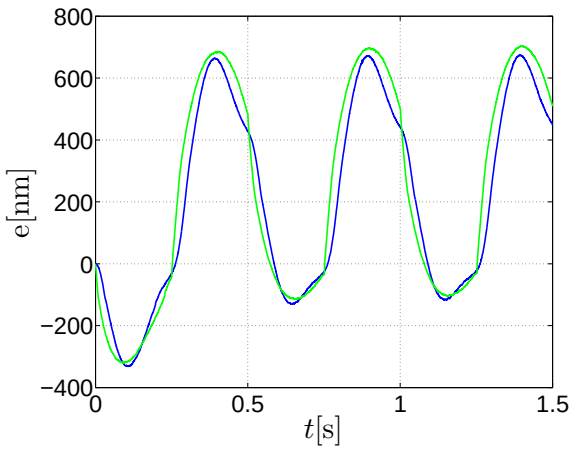

Figure 6.6: Displacement error to 2 Hz normalized sinusoidal (blue) and triangular (green) inputs.

6.4 Rate-independent hysteresis models

Following simulations are performed with rate-independent hysteresis models only, neglecting any electro-mechanical properties of the stack actuator. Two models introduced in Chapter 5 are identified, simulated and compared with measured data.

Al Janaideh's Prandtl–Ishlinskii model

Only one parameter is chosen before performing least-squares fit – number of hysteresis operators. Increasing the number of hysteresis operators produces noticeable improvement only up to 10 operators. The parameters of this model are:

$$\begin{aligned} J &= 10, & q &= 18.42, & \beta &= 0.047, \\ \alpha &= 8.11, & \sigma_r &= 5.28, & c &= 1.21. \end{aligned} \tag{6.2}$$

Ang's Prandtl–Ishlinskii model

Experiments shown that the best results compared to a reasonable amount of parameters that describe the model is 12 for the number of hysteresis operators and just 1 deadzone operator, excluding the zero width operators. The backlash operator widths r are chosen to be equidistant between 0 to 50 V with interval σ_r. The parameters of this model are:

$$\begin{aligned} \sigma_r &= 4.17, \\ \mathbf{d} &= \begin{bmatrix} 0 & 342.58 \end{bmatrix}, \\ \mathbf{w_s}^{\mathrm{T}} &= \begin{bmatrix} 1.47 & 0.21 \end{bmatrix}, \end{aligned} \tag{6.3}$$

$$\mathbf{w_f}^{\mathrm{T}} = \begin{bmatrix} 9.84 & 11.13 & 1.26 & 2.04 & 1.27 & 1.45 & 1.16 & 1.20 & 1.09 & 0.85 & 1.38 \end{bmatrix}.$$

Comparison

Sinusoidal input at 2 Hz frequency was used for parameter identification. Fig. 6.7 shows the hysteresis loops of both models. A validation was performed by triangular input signal at the same frequency. In Fig. 6.8 we can see the results shown as time graphs.

Model	Al Janaideh's		Ang's	
Input	Sinusoidal	Triangular	Sinusoidal	Triangular
Maximum error [nm]	86.17	76.79	72.50	86.92
RMSE [nm]	33.88	39.21	28.63	34.05

Table 6.3: Measured errors of Al Janaideh's and Ang's models. Maximum errors are measured after the error steadies, i.e. after two periods of input signal.

These figures show that both models fit the measured data very well, with bigger error only at the extremes. To see the error between measured data and the models better, it is plotted in Fig. 6.9. Ang's model has lower root mean square error and also lower maximum error than Al Janaideh's model in all measurements and is therefore slightly better. The errors are summarized in Table 6.3.

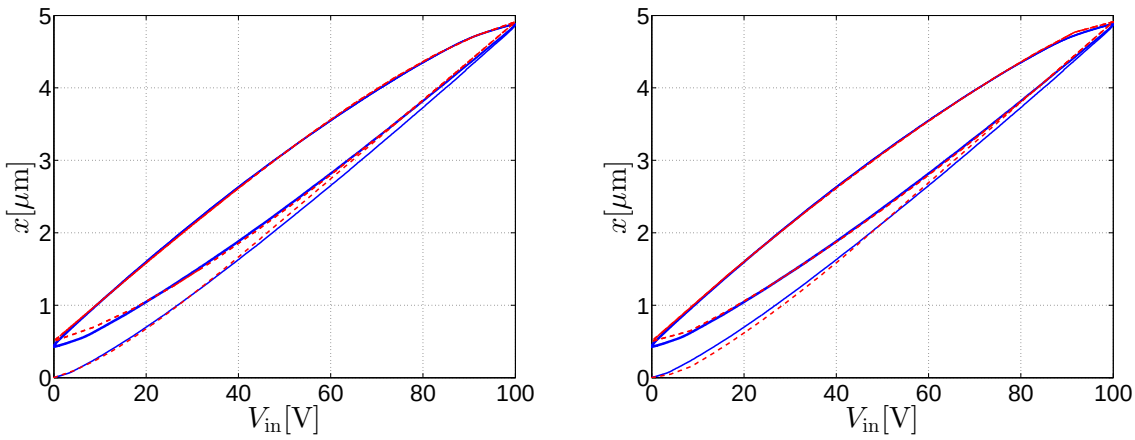

(a) Al Janaideh's model **(b)** Ang's model

Figure 6.7: Comparison of hysteresis models (red) and measured data (blue).

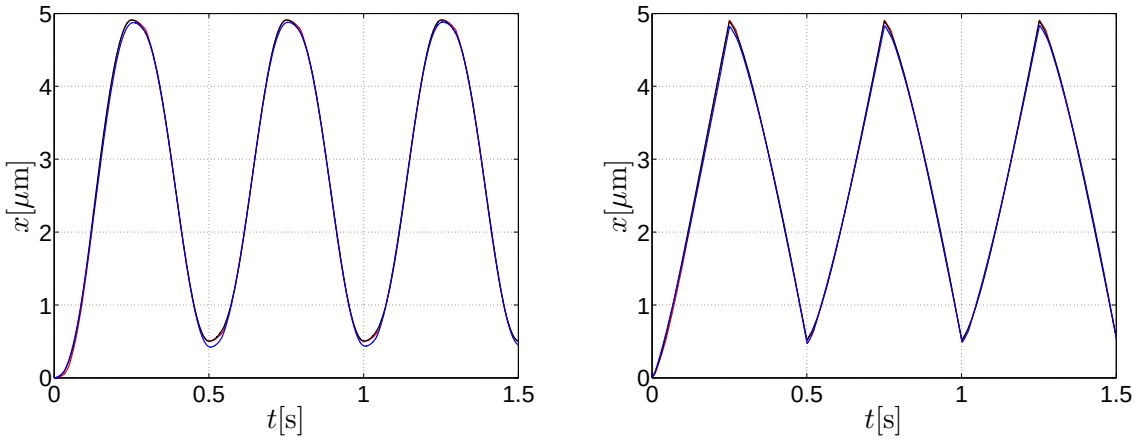

(a) Sinusoidal input **(b)** Triangular input

Figure 6.8: Time graphs of measured data for sinusoidal and triangular inputs, blue line is the measured displacement, black line is Al Janaideh's model output and red line is Ang's model output.

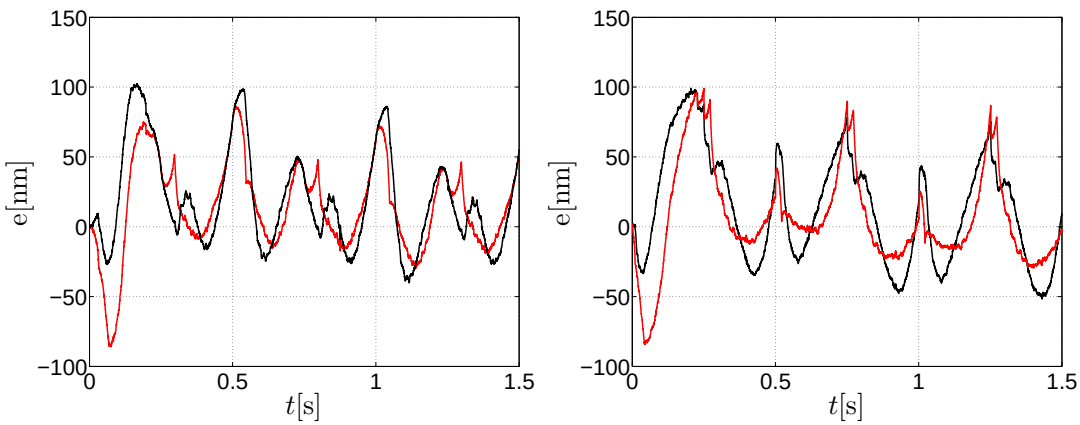

(a) **(b)**

Figure 6.9: Displacement error of Al Janaideh's (black) and Ang's (red) models.

6.5 Complete mechanical and hysteresis models

In this section simulations of two complete electro-mechanical stack actuator models with hysteresis model included are performed and compared with the measured data.

General bond graph model with Ang's Prandtl–Ishlinskii hysteresis model

General bond graph model is a great framework for modeling piezoelectric stack actuators with hysteresis. Hysteresis is modeled in the polarization domain as a nonlinear compliance C_{nl}. We can mathematically write this:

$$E_{\mathrm{C}} = C_{\mathrm{nl}}(p), \tag{6.4}$$

where E_{C} is electric field and p is electric dipole. This approach allows various hysteresis models to be included. On the following lines a combination of this model with Ang's hysteresis model is presented.

From equations 5.3 we can derive formulas to compute electric dipole and electric field at the compliance C_{nl} from the measured displacement x and input voltage V_{in}:

$$\begin{aligned} p &= \frac{\ell}{kT}\left(m\ddot{x} + kx\right), \\ E_{\mathrm{C}} &= \frac{V_{\mathrm{in}}}{\ell} - \left(\frac{R_{\mathrm{e}}m}{kT\ell}\dddot{x} + \frac{mT}{\ell}\ddot{x} + \frac{R_{\mathrm{e}}}{T\ell}\dot{x}\right). \end{aligned} \tag{6.5}$$

The hysteresis is included in the general bond graph model as a function with electric dipole at the input and electric field at the output. This function can't be directly identified for Ang's model, but its inverse $p = f(E_{\mathrm{C}})$ can. The obtained model's parameters can then be inverted to fit Ang's inverse model, which is capable of modeling the $E_{\mathrm{C}} = f(p)$ loop. The hysteresis loop is plotted in Fig. 6.11. The parameters of the Ang's inverse model are:

$$\begin{aligned} \mathbf{r} &= \begin{bmatrix} 0 & 0.55 & 1.82 & 3.17 & 4.62 & 6.16 & 7.79 & 9.48 & 11.23 & 13.08 & 15.01 & 16.94 & 18.89 \end{bmatrix}, \\ \mathbf{w_f}^{\mathrm{T}} &= [\, 4.2\times10^{-1} \;\; -2.4\times10^{-1} \;\; -9.4\times10^{-3} \;\; -1.2\times10^{-2} \;\; -9.6\times10^{-3} \ldots \\ &\quad \ldots -7.8\times10^{-3} \;\; -5.2\times10^{-3} \;\; -5.4\times10^{-3} \;\; -6.0\times10^{-3} \;\; -5.7\times10^{-3} \ldots \\ &\quad \ldots -5.0\times10^{-4} \;\; -1.0\times10^{-4} \;\; -2.0\times10^{-6} \,], \\ \mathbf{d} &= \begin{bmatrix} 0 & 2.51 \end{bmatrix}, \qquad \mathbf{w_s} = \begin{bmatrix} 16.81 & -12.32 \end{bmatrix}, \end{aligned}$$

The inverting algorithm is described later in Chapter 7, where it is used to create inverse hysteresis model to compensate the hysteresis. Based on eq. 5.4 a Simulink model was created and the hysteresis model validated. Since the least-squares algorithm in Matlab is sensitive to difference in magnitude of input and output data, the electric dipole and electric field were multiplied by 1×10^{8} and 1×10^{-3}, respectively, to allow successful curve fitting. This explains the gain blocks surrounding the hysteresis block in the Simulink model shown in Fig. 6.10.

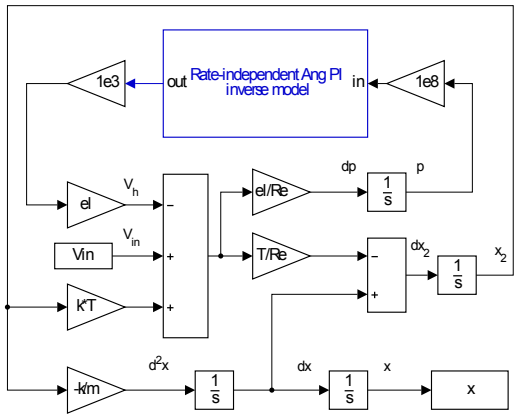

Figure 6.10: Simulink implementation of the General bond graph model for piezo stack actuators with Ang's inverse hysteresis model.

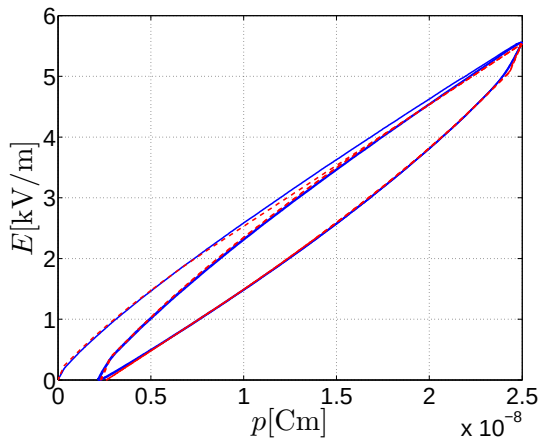

Figure 6.11: Hysteresis loop between electric dipole and electric field at the nonlinear compliance C_{nl} of the General bond graph model.

Nonlinear lumped-parameter model with Maxwell resistive capacitor hysteresis model

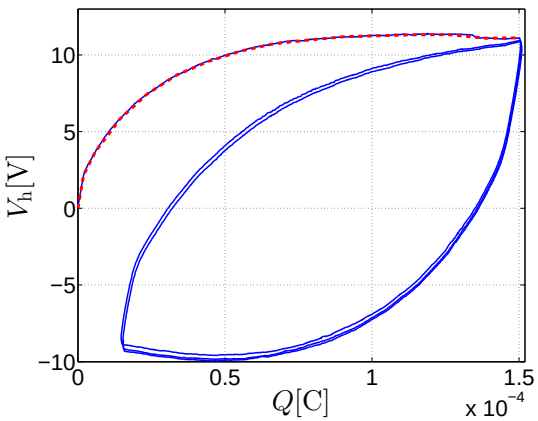

Figure 6.12: Hysteresis loop (blue) between charge and voltage V_{h} modeled by Maxwell resistive capacitor and least-squares fit of the loading curve (red).

i	C_i [μC/V]	v_i [V]
1	1.37	1.42
2	7.83	0.75
3	12.34	1.16
4	19.06	1.24
5	25.25	1.33
6	44.63	0.99
7	56.52	0.98
8	46.89	1.42
9	229.64	0.34
10	94.60	0.95
11	447.08	0.23
12	342.68	0.33
13	50.20	2.52
14	49.56	2.80
15	616.13	0.24

Table 6.4: Maxwell resistive capacitor model parameters.

The principle of including hysteresis has some similarities with the previous model. Measured displacement and input is transformed to charge q and voltage over the hysteresis element V_{h}. From eq. 5.1 we can derive the equations 6.6 that can be directly implemented

in Simulink to obtain the required quantities:

$$\begin{aligned} V_{\mathrm{h}} &= V_{\mathrm{in}} - \frac{1}{T}\left(m\ddot{x} + b\dot{x} + kx\right), \\ q &= Tx + \frac{C}{T}\left(m\ddot{x} + b\dot{x} + kx\right) \end{aligned} \tag{6.6}$$

The Maxwell resistive capacitor hysteresis model is included as a nonlinear function H.

$$V_{\mathrm{h}} = H(q) \tag{6.7}$$

Fig. 6.12 shows the hysteresis loop including the loading curve and its piecewise linear fit over 15 segments. Table 6.4 summarizes the parameters C_i and v_i that were obtained by following the procedure described in Chapter 5. The whole model was, similarly to the model above, implemented in Simulink.

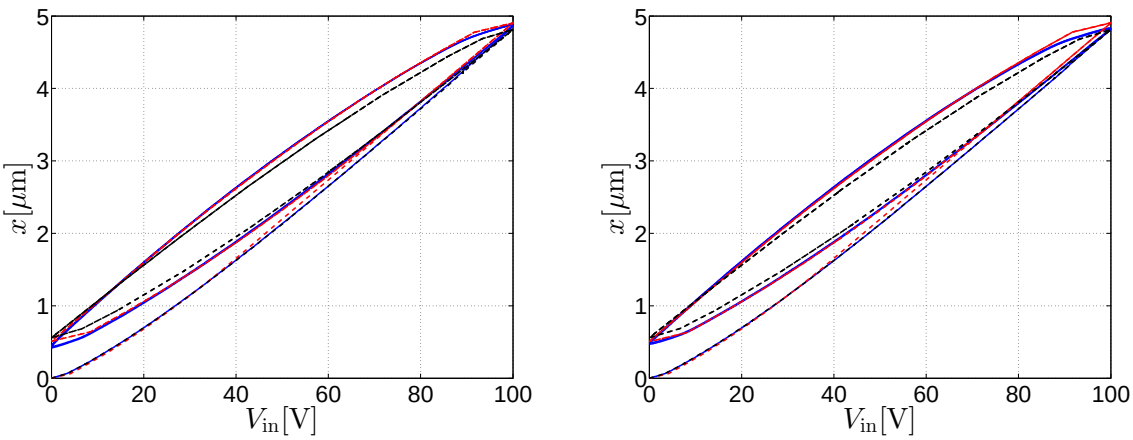

(a) Sinusoidal input **(b)** Triangular input

Figure 6.13: Hysteresis loops for sinusoidal and triangular inputs – measured data (blue), General bond graph model (red), Nonlinear lumped-parameter model (black).

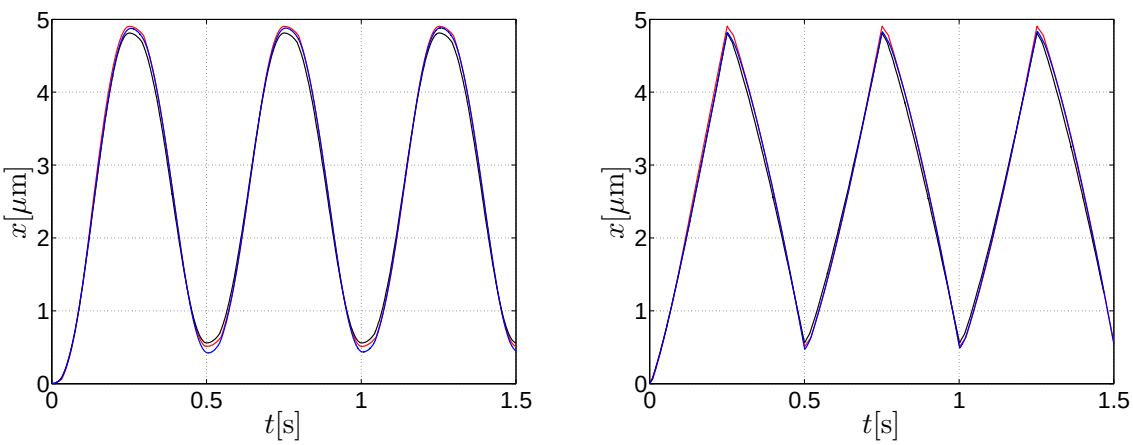

(a) Sinusoidal input **(b)** Triangular input

Figure 6.14: Displacement plotted in time for sinusoidal and triangular inputs – measured data (blue), General bond graph model (red), Nonlinear lumped-parameter model (black).

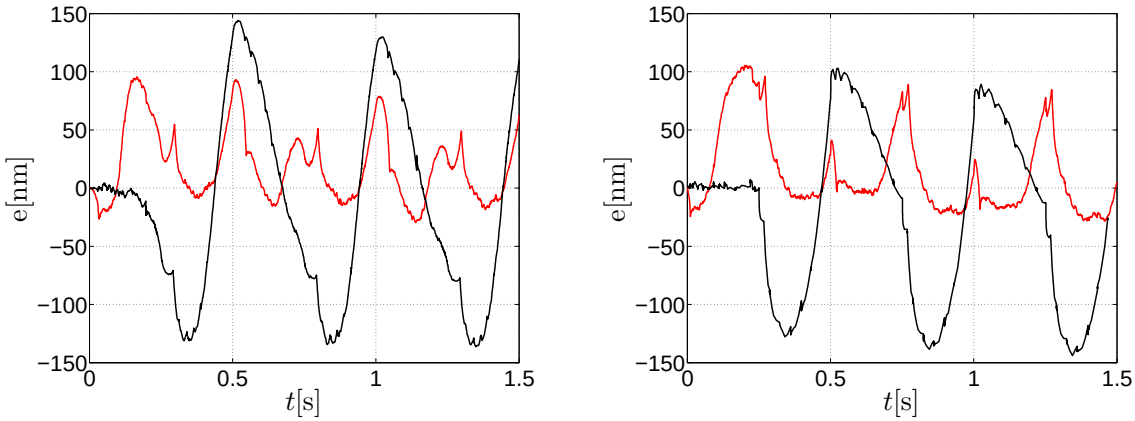

(a) Sinusoidal input **(b)** Triangular input

Figure 6.15: Displacement error of General bond graph (red) and Nonlinear lumped-parameter (black) models.

Model	General bond graph		Nonlinear lumped-parameter	
Input	Sinusoidal	Triangular	Sinusoidal	Triangular
Maximum error [nm]	95.51	105.35	167.31	163.3
RMSE [nm]	29.59	35.44	87.36	83.69

Table 6.5: Measured errors of General bond graph and Nonlinear lumped-parameter models.

Comparison

General bond graph model with Ang's hysteresis model has been identified for 2 Hz sinusoidal input and the Nonlinear lumped-parameter model with Maxwell resisitive capacitor for 2 Hz triangular signal. From the hysteresis loops shown in Fig. 6.13 we can see that the first model fits nearly perfectly, while the second model's results are good, but considerably worse in comparison. The difference between results with sinusoidal and triangular signals is minimal. Both models are better with the input they were identified for. Fig. 6.15 shows the displacement error of both models and Table 6.5 summarizes the maximum and root mean square error for all measurements.

6.6 Problems

The biggest problem encountered was with the synchronization of input data and the measured values read from the interferometer. The signal processing module of the interferometer is not able to process and send the data sufficiently fast to enable real-time operation. Therefore, the measurement has to be performed in superfast mode – interferometer upon receiving starting trigger pulse starts to measure with a preset sampling frequency and saves the data in the internal memory. After the measurement is finished the data is sent to the PC. The problem is, that there is a small difference in sampling frequency in Simulink and sampling frequency of the interferometer, even though they are set to be the same. Fig. 6.16 shows a hysteresis loop created by input and output

signals with slightly different frequency. The interferometer can't be triggered for each data point in the superfast mode and thus the problem was solved by resampling the input data before matching them with the measured values. The solution of this problem is not optimal, it is not accurate and it distorts the results. When performing measurements with higher frequency input signal, while maintaining the same sampling frequencies, the difference in sampling frequencies appeared to vary in time. Due to this problem it is impossible to measure, identify and implement rate-dependent hysteresis models.

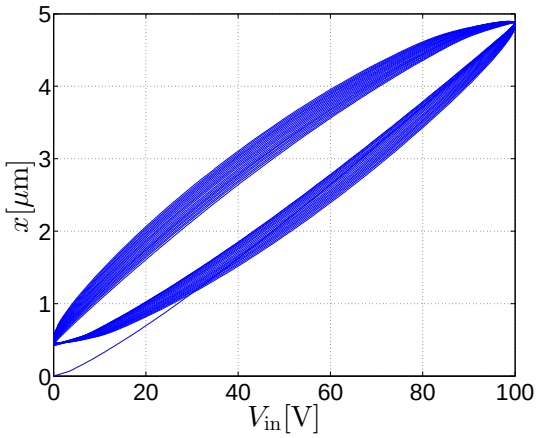

Figure 6.16: Hysteresis loop created with unsynchronized input and output sampling.

Let me mention the fact, that the actuator available for measurements was achieving displacements only up 4.9 µm, which is a third of the expected displacement given by the documentation. This did not turn up to be a problem for modeling.

For complete mechanical models with hysteresis included I encountered numerical problems in Simulink models caused by algebraic loops created by the hysteresis models and by having signals with big difference in magnitude, such as charge and voltage, or even worse – electric dipole and electric field with a difference of 11 orders. The only Matlab solver that was able to run the simulation in reasonable time was *ode23tb*.

6.7 Conclusion

Measurements showed, that all the hysteresis and stack actuator models fit the real actuator very well. Ang's Prandtl–Ishlinskii hysteresis model achieved the best results of the three hysteresis models developed. The main reason for its better performance than Al Janaideh's Prandtl–Ishlinskii model is the ability to model asymmetrical hysteresis. Even though the stack actuator available did not demonstrate strong asymmetry, using the Ang's model proved slightly better. The third model, Maxwell resistive capacitor, is considerably worse in every aspect than the Prandtl–Ishlinskii models. This is caused by the way the parameters of the model are identified, Prandtl–Ishlinskii models use least-squares linear fit over all measured data, while the Maxwell resistive capacitor acquires the parameters by piecewise linear fit of the loading curve only. To achieve best results, there should be no remanent hysteresis when measuring the loading curve. Even application of 'cleaning' signal beforehand does not guarantee a hysteresis free actuator at the start of the measurement.

A comparison of Generalized bond graph model and Nonlinear lumped-parameter model from the measured results is impossible, due to the presence of hysteresis model. Generalized bond graph model is more powerful in terms of modeling abilities. It is able to include further nonlinear phenomena such as creep and even model rate-dependency while using rate-independent hysteresis models. In terms of practical Simulink implementation the Nonlinear lumped parameter model was easier to implement and simulate.

Chapter 7

Control and hysteresis compensation of stack actuator

This chapter is dedicated to hysteresis compensation of piezoelectric stack actuators. After giving survey of existing stack actuator control and hysteresis compensation approaches, two inverse Prandtl–Ishlinskii models and an inverse of Nonlinear lumped-parameter model are simulated as feedforward hysteresis compensators and the results compared with Physik Instrumente's P-840.1 actuator measurements.

7.1 A survey of existing hysteresis compensation and stack actuator control approaches

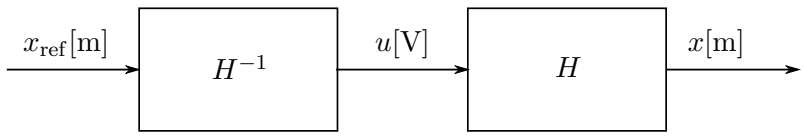

Figure 7.1: Hysteresis compensation as a feedforward inverse of the hysteresis model.

The basic concept of hysteresis compensation is shown in Fig. 7.1. An inverse of hysteresis model is used as a feedforward controller that produces voltage input to the actuator from a given displacement reference. The first inverse hysteresis models for piezoelectric actuators were studied by Kuhnen, Janocha and Krejčí [32, 33] at the end of 1990's. For hysteresis compensation and control purposes Prandtl–Ishlinskii models are very popular owing to their analytical invertibility. W. Ang's [23] and O. Al Janaideh's [34] modifications of Prandtl–Ishlinskii hysteresis model and their inverses are discussed in this project. There are several approaches to improve the quality of compensation with inverse hysteresis model. Tan [35], Chen [36] and others use adaptive control to manipulate the weights of the hysteresis operators during operation to match them better with reality. Tzen [37] models the actuator as a hysteresis followed by linear second order system. He compensates the hysteresis with feedforward controller and controls the actuator with PI feedback controller. Lee [38] uses a feedback sliding mode controller together with the hysteresis inverse.

7.2 Hysteresis compensation

A simple feedforward hysteresis inverse compensation, shown in Fig. 7.1 is tested on two Prandtl–Ishlinskii hysteresis models, introduced in Chapter 5, identified and compared with real actuator behavior in Chapter 6. All electro-mechanical properties of the actuator are neglected, the actuator is modeled by hysteresis model only. The notation used is consistent with the notation used in previous chapters.

Al Janaideh's Prandtl–Ishlinskii model

The inverse density parameters Θ'_j and inverse backlash operator widths r'_j can be obtained by applying following algorithm on identified parameters of the hysteresis model:

$$\begin{aligned} \Theta'_j &= \frac{-\Theta_j}{\left(q + \sum_{i=1}^{j} \Theta_i\right)\left(q + \sum_{i=1}^{j-1} \Theta_i\right)}, \\ r'_j &= q r_j + \sum_{i=1}^{j} \Theta_i (r_j - r_i), \end{aligned} \tag{7.1}$$

where $j = 1, \ldots, J$.

Ang's Prandtl–Ishlinskii model

The inverting algorithm for Ang's model is more complicated than Al Janaideh's due to the presence of one-sided deadzone operators. We can write it:

$$\begin{aligned} w'_{\mathrm{f}_0} &= \frac{1}{w_{\mathrm{f}_0}}, \\ w'_{\mathrm{f}_i} &= \frac{-w_{\mathrm{f}_i}}{\left(\sum_{j=0}^{i} w_{\mathrm{f}_j}\right)\left(\sum_{j=0}^{i-1} w_{\mathrm{f}_j}\right)}, && \text{for } i = 1, \ldots, J \\ r'_i &= \sum_{j=0}^{i} w_{\mathrm{f}_j} (r_i - r_j), && \text{for } i = 0, \ldots, J, \\ w'_{\mathrm{s}_0} &= \frac{1}{w_{\mathrm{s}_0}}, \\ w'_{\mathrm{s}_i} &= \frac{-w_{\mathrm{s}_i}}{\left(\sum_{j=0}^{i} w_{\mathrm{s}_j}\right)\left(\sum_{j=0}^{i-1} w_{\mathrm{s}_j}\right)}, && \text{for } i = 1, \ldots, m \\ d'_i &= \sum_{j=0}^{i} w_{\mathrm{s}_j} (d_i - d_j), && \text{for } i = 0, \ldots, m \end{aligned} \tag{7.2}$$

where apostrophe denotes inverse parameters.

Simulation, measurement and comparison

Model parameters identified in Chapter 6 were inverted by the algorithms above and the resulting inverse models were simulated for following reference displacement signal:

$$x_{\mathrm{ref}} = \begin{cases} 2000 \sin(2\pi t - \frac{\pi}{2}) + 2000 & \text{for } t \in \langle 0, 0.5), \\ 1500 \sin(2\pi t - \frac{\pi}{2}) + 2500 & \text{for } t \geq 0.5. \end{cases} \tag{7.3}$$

The voltage obtained was then used as an input to the actuator. Fig. 7.2 compares the results between simulated model and the measured data. Feedforward controller output voltages are plotted in Fig. 7.3. From the results we can see that the inverses of both models perfectly compensate the hysteresis in simulations and also a compensation of real actuator's hysteresis is very good. The hysteresis virtually disappears, but there is a small tracking error, especially around 1µm reference. Since Ang's hysteresis model was found to be slightly better than Al Janaideh's, it was expected that Ang's feedforward controller would also be better and the results confirm that.

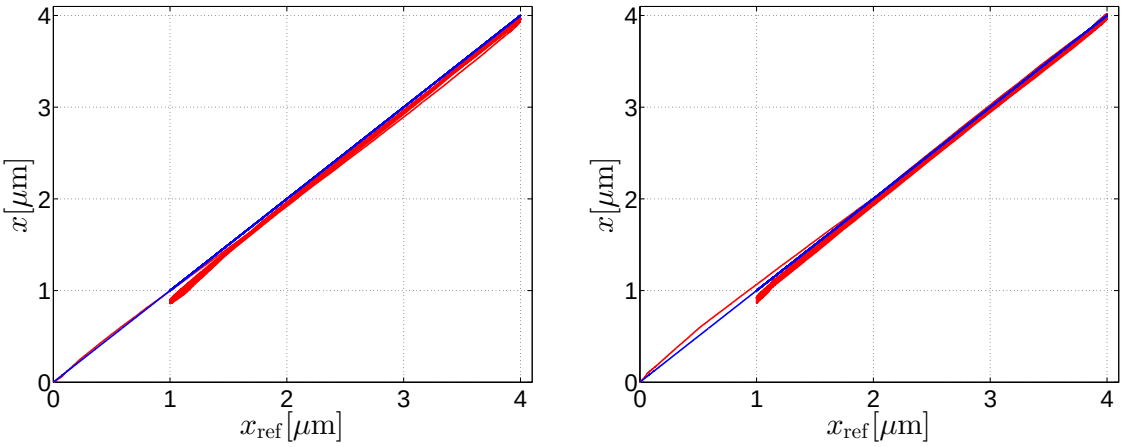

(a) Al Janaideh's model **(b)** Ang's model

Figure 7.2: Hysteresis compensation of Prandtl–Ishlinskii hysteresis models – simulated (blue), inverse feedforward with real actuator (red).

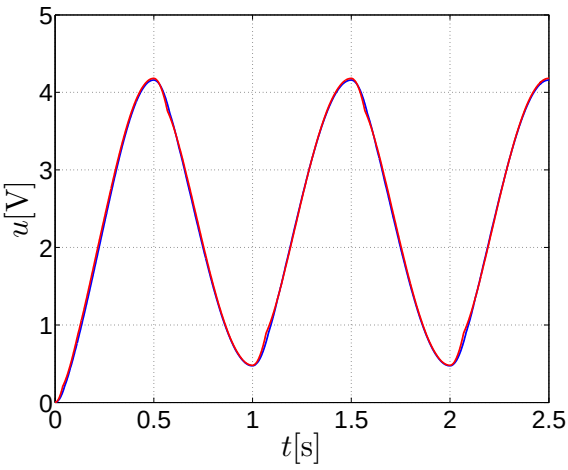

Figure 7.3: Inverse hysteresis feedforward controller output – Al Janaideh's (blue), Ang's(red).

7.3 Nonlinear lumped-parameter model hysteresis compensation

This model combines electro-mechanical properties of the actuator with a Maxwell resistive capacitor hysteresis model included. The hysteresis can be compensated by inverting

whole model as is shown by Simulink model in Fig. 7.4. The displacement reference signal used is given by eq. 7.3. The corresponding reference velocity and reference acceleration could be determined by numerical differentiation of the reference displacement, but this is inadvisable since the numerical differentiation creates noise in the system and for certain initial values creates peaks that are several orders of magnitude higher than rest of the signal. A preferred approach is to create analytical derivatives of the displacement if possible.

The results depicted in Fig. 7.5 show that the feedforward controller proposed compensates the hysteresis model perfectly. The hysteresis compensation results with real stack actuator are slightly worse than those discussed in the previous section. Hysteresis loop is not entirely compensated, it is approximately 0.11 µm thick in its thickest point, which is less than 4% of the displacement range. The reason for the worse result is the model, which was not identified to fit the measured data perfectly. Nevertheless, the result is very good.

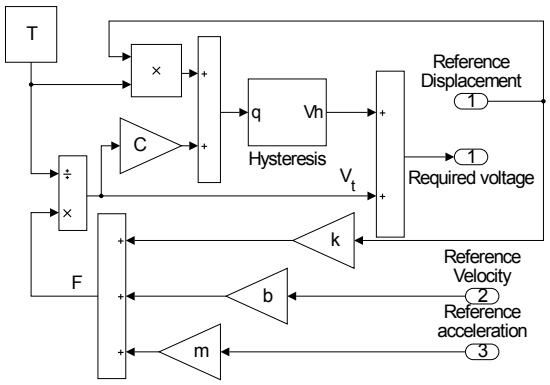

Figure 7.4: Simulink model of feedforward inverse of Nonlinear lumped-parameter model with Maxwell resistive capacitor hysteresis model.

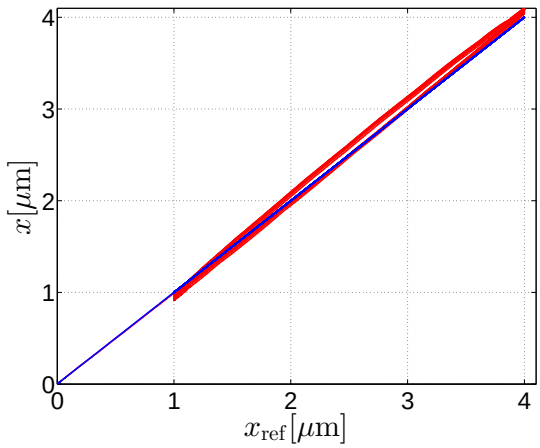

Figure 7.5: Feedforward compensation by Nonlinear lumped-parameter model inverse.

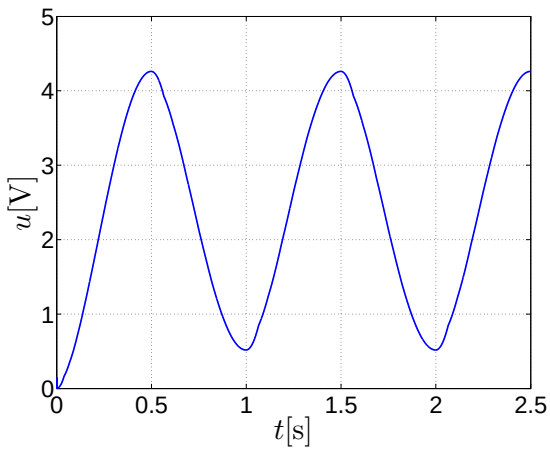

Figure 7.6: Inverse Nonlinear lumped-parameter model output.

Chapter 8

Ultrasonic actuator

Commercially available ultrasonic plate actuator M-661 is examined in this chapter from practical point of view. At the beginning a simple model of the actuator is suggested. This is followed by a discussion of experimental results, namely input-output characteristics, measurement of the three-wire signal fed to the actuator by driver electronics, and step response behavior. The chapter is concluded by discussion of problems encountered.

8.1 Modeling

For practical purposes it is often sufficient to use simple models of actuators. This approach has been chosen by T. Villgrattner [39] with his dynamic camera orientation system, where he uses a similar actuator to M-661. The following model, depicted in Fig. 8.1 is inspired by his approach.

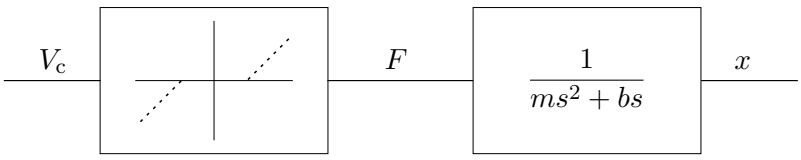

Figure 8.1: Model of ultrasonic plate actuator.

The driver electronics and the actuator, considered as one system, are modeled as a deadzone operator between control voltage V_c and output force F followed by a mass-damper system representing a movable stage of the actuator showed in Fig 8.2.

8.2 Measurements

8.2.1 Voltage-force dependence

Nonlinearity between input and output is one of the biggest disadvantages of this actuator. Fig. 8.3 shows the dependence between control voltage to the driver electronics and a force at the output of the actuator. Polarity of the control voltage determines direction of movement, while the amplitude determines velocity and force at the output. The force was measured with DS2-5N Imada force gauge and the data were sent to PC via RS-232/USB converter for processing in Matlab. The measurement was performed for positive voltage only and was mirrored for negative input. In the results we can see a big deadzone, which

is approximately 2 V wide in each movement direction. Closely after the deadzone the output force rises quickly to reach its maximum around 6 V of input voltage, which is only 60% of the voltage range for movement in one direction.

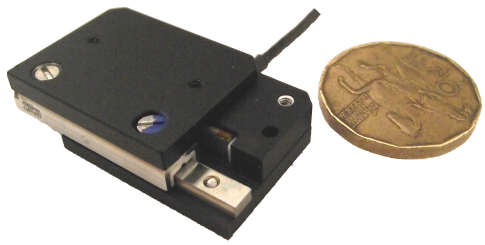

Figure 8.2: M-661 ultrasonic actuator in its maximal displacement.

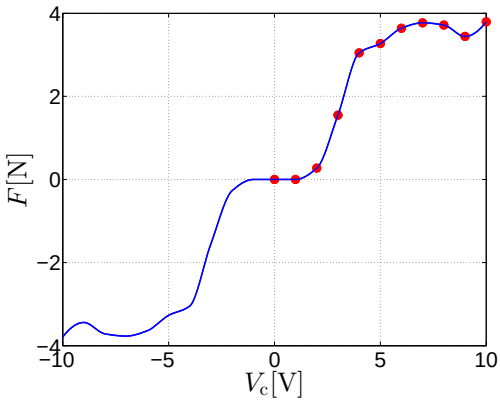

Figure 8.3: Nonlinear voltage-force dependence of the ultrasonic actuator driven by C184.161 driver electronics.

8.2.2 Actuator's three-wire input

This measurement was performed to determine the shape of signal sent by the C-184.161 driver electronics to the M-661 ultrasonic actuator. The input of the actuator is a 215 kHz three-wire signal. Each of the signals is connected to one of the three electrodes attached to the piezoceramic element shown in Fig. 8.5. In Fig. 8.4 we can see a detailed view of the driver electronics outputs. The P1 output carries signal for the back electrode and the P2 and P3 outputs control the front electrodes. To determine the voltage between the electrodes, the signals were measured against the ground and then the back electrode voltage was subtracted. The results are shown in Fig. 8.6 and 8.7.

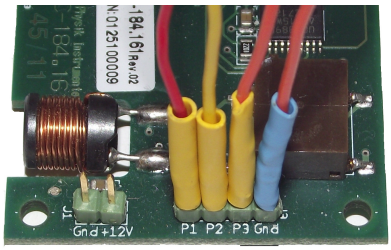

Figure 8.4: Output pins of the C-184.161 driver electronics.

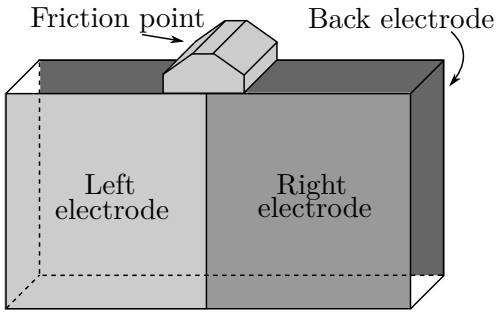

Figure 8.5: Electrode layout of the M-661 ultrasonic actuator.

8.2.3 Step response to control voltage

A response to control voltage input step is very nonlinear. It depends on direction of polarity change as well as magnitude of the step. From the results shown in Fig. 8.8 we can see that the settling time nearly doubles when performing step from −9 V to 9 V compared to smaller step from −4 V to 4 V. Due to the piezoceramic properties the

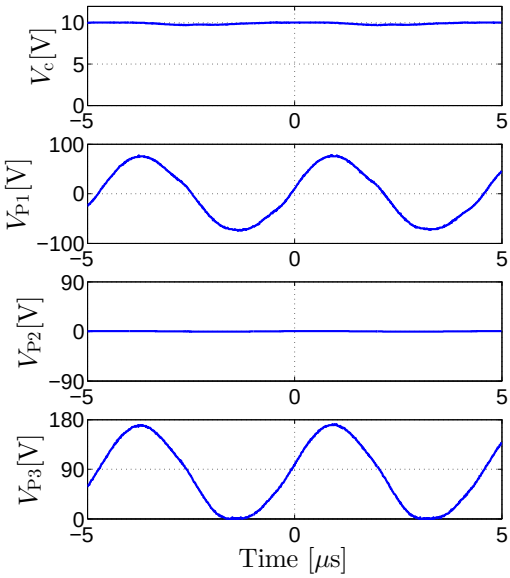

Figure 8.6: Output of the driver electronics measured against the ground when maximum control voltage V_c is used.

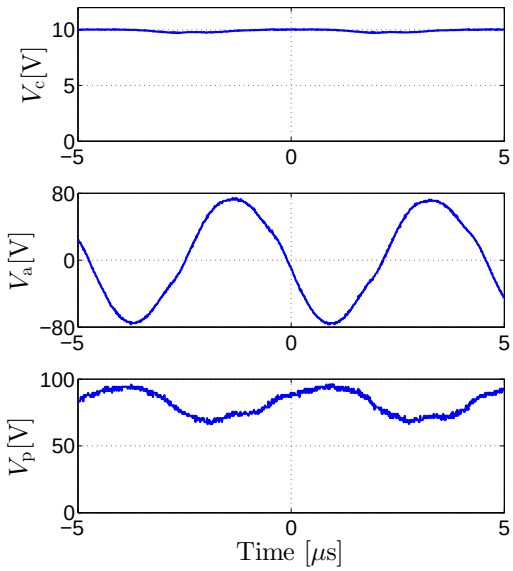

Figure 8.7: Voltage between front electrodes and the back electrode. V_a denotes active electrode voltage and V_p passive.

actuator responds faster in one direction. Settling time after step in the opposite direction than in Fig. 8.8b is approximately 0.1 ms longer.

8.3 Problems and discussion

There are several problems that complicate interaction with M-661 ultrasonic actuator. The biggest problem is the nonlinear input-output characteristic, which complicates using the actuator for slow velocities. Another problem is a low stability of output for particular input. This makes it virtually impossible to use with open loop control. The output stability is lower for lower velocities and is also affected by position of the stage. To give an example of this behavior – setting a 3 V input, which is sligthly more than a deadzone boundary, can result in no output whatsoever or the actuator could start moving and get stuck before getting to the maximum displacement. This behavior makes it very complicated for measuring with interferometer. The measurement requires precise alignment of the beam leaving the interferometer and the one reflected back from the actuator. Since small velocities are hard to achieve, greater velocities move the actuator over longer displacement range, which is difficult to get the interferometer aligned to. Force measurement is considerably easier to carry out, but is not without problems either. Due to the instability of output the results had to be avaraged with outliers excluded. Fig. 8.9 shows a force measurement over a period of one second with 100 Hz sampling rate and control voltage set to 10 V.

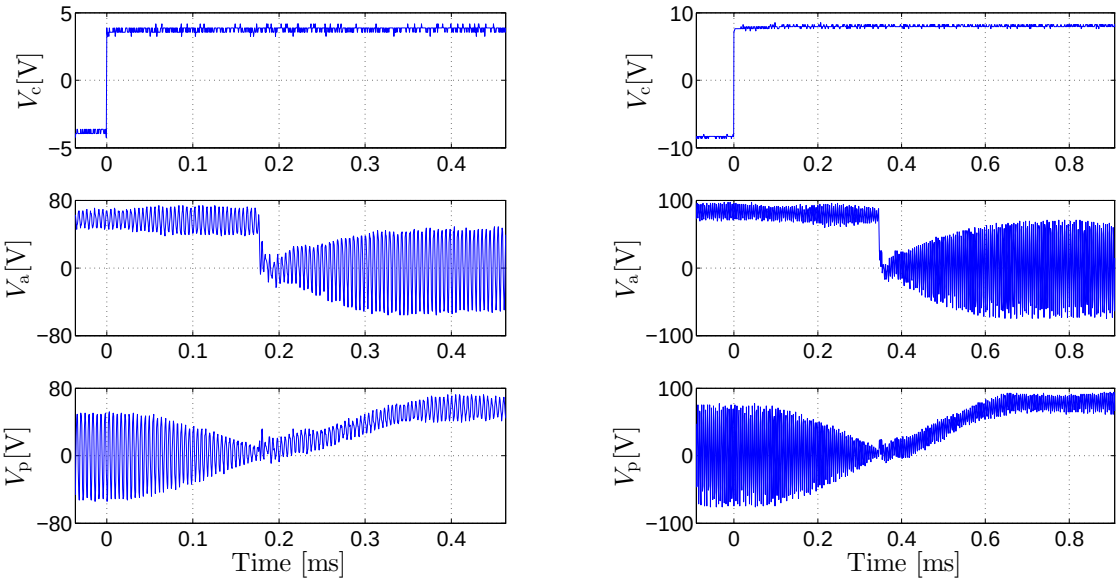

Figure 8.8: Driver electronics step response. The settling time in (b) is approximately two times longer than in (a).

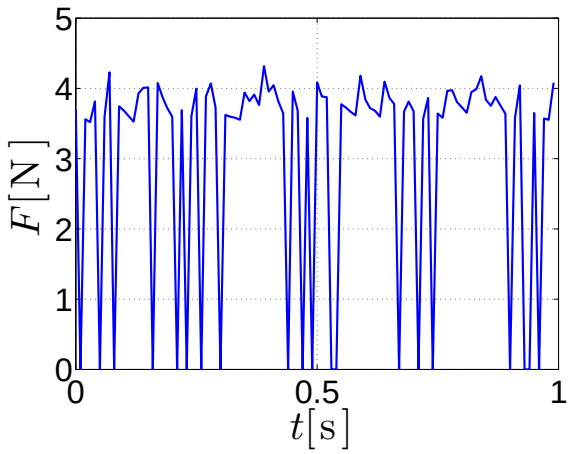

Figure 8.9: Force measurement of the ultrasonic actuator for 10 V control voltage.

Chapter 9

Conclusion

Simulations and measurements of real stack actuator showed that all the models introduced in Chapter 5 and created as a combination of ideas drawn from several journal articles are very good mathematical representations of the physical device. Prandtl–Ishlinskii hysteresis models were confirmed to be very accurate, while reasonably difficult to identify for hysteresis of the real actuator. Owing to their main advantage – analytical invertibility – perfect model inverses can be developed. These inverses were used as feedforward hysteresis compensators and very good results were obtained with real stack actuator. For more details about stack actuator simulations and measurements see conclusion at the end of Chapter 6. Outcomes of hysteresis compensation are thoroughly discussed throughout the Chapter 7.

There were several problems that influenced the results presented in this project. Probably the biggest problem were unsynchronized sampling frequencies of input voltage and measured displacement, discussed in more detail in Chapter 6. The proposed solution works fairly well for low rate voltage input only; therefore disallowing modeling of hysteresis as rate-dependent phenomenon. This problem could be solved properly by using a different displacement measuring device that would allow measurements synchronized with generated input voltage. This leaves some possibilities for future work.

Ultrasonic linear plate actuator is a device intended primarily for closed-loop operation. In Chapter 8 it has been shown that the high nonlinearity between input and output together with instability of output for particular input make it very difficult to control in open-loop. Closed-loop control was not possible with the measurement setup available. The main problem was low interferometer sampling rate in real-time operation. Better sampling rates could be achieved by upgrading the data-processing module of the interferometer or replacing the device with another measurement tool. The best solution is purchasing the ultrasonic actuator with position encoder embedded, which would also allow out-of-the-laboratory use of the closed-loop controlled actuator.

With feedback control available there are many possibilities and ideas for future work. For example, resonant frequencies of ultrasonic actuators change in time due to various influences such as heating. The input frequency to the actuator could be matched to the current resonant frequency by using a phase-locked loop.

Bibliography

[1] Wikipedia, "Wikipedia, the free encyclopedia," 2013. [Online]. Available: http://en.wikipedia.org

[2] "Physik instrumente." [Online]. Available: http://www.physikinstrumente.com/en/index.php

[3] Y. Saito, H. Takao, T. Tani, T. Nonoyama, K. Takatori, T. Homma, T. Nagaya, and M. Nakamura, "Lead-free piezoceramics," *Nature*, vol. 432, no. 7013, pp. 84–87, Oct. 2004.

[4] "IEEE standard on piezoelectricity," *ANSI/IEEE Std 176-1987*, p. 0_1, 1988.

[5] "APC international." [Online]. Available: http://www.americanpiezo.com/

[6] "Sensor Technology Ltd." [Online]. Available: http://www.sensortech.ca/site/

[7] M. Špiller and Z. Hurák, "Hybrid charge control for stick–slip piezoelectric actuators," *Mechatronics*, vol. 21, no. 1, pp. 100–108, Feb. 2011.

[8] S. O. R. Moheimani and A. Fleming, *Piezoelectric transducers for vibration control and damping.* London: Springer, 2006.

[9] V. Sharapov, "General information about piezoelectric sensors," in *Piezoceramic Sensors.* Springer, 2011, p. 1–24.

[10] L. E. Cross and R. E. Newnham, "History of ferroelectrics," *J. Am. Ceram.*, vol. 11, p. 289–305, 1987. [Online]. Available: www.ieee-uffc.org/main/history/cross_newnham.pdf

[11] K. Uchino, "Piezoelectric actuators 2006," *Journal of Electroceramics*, vol. 20, no. 3-4, p. 301–311, 2008.

[12] K. Spanner, "Survey of the various operating principles of ultrasonic piezomotors," in *Proceedings of the 10th International Conference on New Actuators*, 2006.

[13] "Ultrasonic motor." [Online]. Available: http://www.seminarseason.com/2012/ultrasonic-motor.html

[14] J. Zumeris, "Ceramic motor." Patent EP0 633 616 (A2), Jan., 1995.

[15] W. Wischnewskiy, "Piezoelectric adjusting element," U.S. Patent 6 765 335, Jul., 2004. [Online]. Available: http://www.freepatentsonline.com/6765335.html

[16] O. Vyshnevsky, S. Kovalev, and W. Wischnewskiy, "A novel, single-mode piezoceramic plate actuator for ultrasonic linear motors," *IEEE Transactions on Ultrasonics, Ferroelectrics and Frequency Control*, vol. 52, no. 11, pp. 2047 –2053, Nov. 2005.

[17] R. Paschotta, "Article on interferometers, Mach-Zehnder, Michelson, Fabry-Pérot, Common-Path - Encyclopedia of Laser Physics and Technology." [Online]. Available: http://www.rp-photonics.com/interferometers.html

[18] G. Jaeger, "Limitations of precision length measurements based on interferometers," *Measurement*, vol. 43, no. 5, pp. 652–658, Jun. 2010.

[19] M. Goldfarb and N. Celanovic, "Modeling piezoelectric stack actuators for control of micromanipulation," *IEEE Control Systems*, vol. 17, no. 3, pp. 69 –79, Jun. 1997.

[20] M. Quant, H. Elizalde, A. Flores, R. Ramírez, P. Orta, and G. Song, "A comprehensive model for piezoceramic actuators: modelling, validation and application," *Smart Materials and Structures*, vol. 18, no. 12, p. 125011, Dec. 2009.

[21] J. Rodriguez-Fortun, J. Orus, F. Buil, and J. Castellanos, "General bond graph model for piezoelectric actuators and methodology for experimental identification," *Mechatronics*, vol. 20, no. 2, pp. 303–314, Mar. 2010.

[22] F. T. Brown, *Engineering System Dynamics: A Unified Graph-Centered Approach, Second Edition*, 2nd ed. CRC Press, Aug. 2006.

[23] W. T. Ang, F. Garmon, P. Khosla, and C. Riviere, "Modeling rate-dependent hysteresis in piezoelectric actuators," in *2003 IEEE/RSJ International Conference on Intelligent Robots and Systems, 2003. (IROS 2003). Proceedings*, vol. 2, Oct. 2003, pp. 1975 – 1980 vol.2.

[24] M. A. Janaideh, S. Rakheja, and C.-Y. Su, "Experimental characterization and modeling of rate-dependent hysteresis of a piezoceramic actuator," *Mechatronics*, vol. 19, no. 5, pp. 656–670, Aug. 2009.

[25] M. Al Janaideh, J. Mao, S. Rakheja, W. Xie, and C.-Y. Su, "Generalized prandtl-ishlinskii hysteresis model: Hysteresis modeling and its inverse for compensation in smart actuators," in *47th IEEE Conference on Decision and Control, 2008. CDC 2008*, Dec. 2008, pp. 5182 –5187.

[26] M. Al Janaideh, C.-Y. Su, and S. Rakheja, "Compensation of rate-dependent hysteresis nonlinearities in a piezo micro-positioning stage," in *2010 IEEE International Conference on Robotics and Automation (ICRA)*, May 2010, pp. 512 –517.

[27] O. Aljanaideh and O. Aljanaideh, "A stop operator-based prandtl-ishlinskii model for compensation of smart actuator hysteresis effects," Thesis, 2009. [Online]. Available: http://spectrum.library.concordia.ca/976756/

[28] "MF624 – Multifunction I/O card user's manual," 2006. [Online]. Available: http://www2.humusoft.cz/www/datacq/manuals/mf624um.pdf

[29] "EPA-104 documentation." [Online]. Available: http://www.piezo.com/prodelect1epa104.html

[30] "P-840 P-841 Preloaded Piezo Actuators." [Online]. Available: http://www.physikinstrumente.com/en/pdf/P840_Datasheet.pdf

[31] L. Juhász, J. Maas, and B. Borovac, "Parameter identification and hysteresis compensation of embedded piezoelectric stack actuators," *Mechatronics*, vol. 21, no. 1, pp. 329–338, Feb. 2011.

[32] K. Kuhnen and H. Janocha, "Adaptive inverse control of piezoelectric actuators with hysteresis operators," in *Proceedings of European Control Conference (ECC)*, 1999. [Online]. Available: http://klauskuhnen.de/images/pdf/ECC99.pdf

[33] P. Krejci and K. Kuhnen, "Inverse control of systems with hysteresis and creep," *IEE Proceedings – Control Theory and Applications*, vol. 148, no. 3, pp. 185–192, 2001.

[34] M. Al Janaideh, S. Rakheja, and C.-Y. Su, "An analytical generalized prandtl-ishlinskii model inversion for hysteresis compensation in micropositioning control," *IEEE/ASME Transactions on Mechatronics*, vol. 16, no. 4, pp. 734 –744, Aug. 2011.

[35] U. X. Tan, W. T. Latt, F. Widjaja, C. Y. Shee, C. N. Riviere, and W. T. Ang, "Tracking control of hysteretic piezoelectric actuator using adaptive rate-dependent controller," *Sensors and Actuators A: Physical*, vol. 150, no. 1, pp. 116–123, Mar. 2009.

[36] X. Chen, "High precision control for piezo-actuated positioners," in *International Conference on Mechatronics and Automation, 2009. ICMA 2009*, 2009, pp. 966–971.

[37] J.-J. Tzen, S.-L. Jeng, and W.-H. Chieng, "Modeling of piezoelectric actuator for compensation and controller design," *Precision Engineering*, vol. 27, no. 1, pp. 70–86, Jan. 2003.

[38] J. Lee, D. Lee, and S. Won, "Precise tracking control of piezo actuator using sliding mode control with feedforward compensation," in *Proceedings of SICE Annual Conference 2010*, Aug. 2010, pp. 1244 –1249.

[39] T. Villgrattner, "Design and control of compact high dynamic camera orientation systems," Ph.D. dissertation, 2010. [Online]. Available: http://nbn-resolving.de/urn:nbn:de:bvb:91-diss-20101021-982079-1-2

[40] A. Bergander, "Control, wear testing & integration of stick-slip micropositioning," Ph.D. dissertation, École polytechnique fédérale de Lausanne, 2003. [Online]. Available: http://dx.doi.org/10.5075/epfl-thesis-2843

Appendix A

SIOS USB library

SIOS provides a *siosusb* library for interacting with interferometer via PC. The main reason for using the library instead of INFAS software, which is provided by the company for the same purposes, is the possibility to work with the interferometer directly through Matlab. SIOS together with the library provides code samples utilizing the library functions in various programming languages, namely C++, Delphi, LabView and already mentioned Matlab. Summary of the provided Matlab files follows. Note here that the *siususb* library offers much more functionality than is achievable using these files. The library together with the samples and provided documentation is included on attached CD.

- **configSIOS_USB_device** — configures the interferometer for running in the normal mode, it is possible to set filtering, averaging and sampling rate.
- **getLengthValue** — returns the last value stored in the interferometer's buffer, works in normal mode only.
- **superfast_sample** — runs superfast mode for chosen sampling frequency and data length, it is possible to set triggering.
- **getEnvirData** — used by superfast_sample, reads environmental data and uses them to correct measured data.
- **unconfigSIOS_USB_device** — unconfigures the interferometer, stops the normal mode.

Appendix B

CD contents

- Simulink and Matlab models of stack actuator
- Matlab scripts for data processing
- data obtained from simulations and measurements
- *siosusb* library for interaction with interferometer via PC, including provided documentation and code samples
- electronic version of the thesis in PDF